Check for updates

Advanced Functional Materials

ADVANCED FUNCTIONAL MATERIALS
www.afm-journal.de

RESEARCH ARTICLE

Knitting Multistability

Kausalya Mahadevan[1] | Michelle C. Yuen[2] | David T. Farrell[1] | Conor J. Walsh[1] | Vanessa Sanchez[3] | Robert J. Wood[1] | Katia Bertoldi[1]

[1]John A. Paulson School of Engineering and Applied Sciences, Harvard University, Cambridge, Massachusetts, USA | [2]Department of Mechanical & Industrial Engineering, Montana State University, Bozeman, Montana, USA | [3]Department of Mechanical Engineering, Rice University, Houston, Texas, USA

Correspondence: Kausalya Mahadevan (kmahadevan@g.harvard.edu) | Katia Bertoldi (bertoldi@seas.harvard.edu)

Received: 2 April 2026 | **Revised:** 21 May 2026 | **Accepted:** 28 May 2026

Keywords: curved shells | knit textiles | multistability

ABSTRACT

Curved elastic shells can be fabricated through molding or by harnessing residual stresses. These shells often exhibit snap-through behavior and multistability when loaded. We present a unique way of fabricating curved elastic shells that exhibit multistability and snap-through behavior, weft-knitting. The knitting process introduces internal stresses into the textile sheet, which lead to complex 3D curvatures. We explore the relationship between the geometry and the mechanical response, identifying a parameter space where the textiles are multistable. We harness the snapping behavior and shape change through multistability to design soft conductive switches with built-in haptic feedback and incorporate these textile switches into two wearable devices and one reconfigurable lamp. This work will allow us to harness the nonlinear mechanical behavior of textiles to create functional, soft, and seamless devices.

1 | Introduction

Elastic shells – thin and curved structures [1, 2] – are ubiquitous in nature and technology, from blood cells and eggs to pressure vessels and roof structures. Across length scales, they are characterized by nonlinear mechanical behavior (e.g., buckling) and are prone to mechanical instabilities [3–6]. While traditionally considered precursors to failure, these instabilities can be harnessed for functionality in elastic shells [7, 8]. Leveraging the snapping behavior of elastomeric shells has led to jumpers [9], swimmers [10–12], programmable fluids [13], and passive valves [14]. Elastic shells with a low thickness-to-radius ratio also exhibit two stable configurations, a characteristic that has been exploited to realize switchable optical lenses [15], valves for autonomous control of soft actuators [16], and the manipulation of the propagation of transition waves [17].

A variety of strategies are used to fabricate curved shells. Some shells are directly built so that the curved shape is their stress-free state [18, 19]. In others, curvature arises in initially flat sheets due to the residual stresses introduced by growth [20, 21], swelling [22, 23], or mechanical loading [24, 25]. Complex shapes, including helices and saddles [24, 26, 27], have been realized by adhering elastic sheets stretched in different directions before releasing the resulting multilayer structures. Increasing the complexity of these shapes would require adhering elastic sheets under more complex strain fields, likely requiring artisanal or one-off processes.

A promising method in creating complex surfaces and designer strain fields while maintaining automated and scalable fabrication is to leverage existing textile manufacturing [28]. We seek to expand these manufacturing technologies, which have been used to create garments for thousands of years to also create wearable devices that make use of multistable curved elastic shells.

Recent research has begun to shed light on the origins of curvature in knit fabrics, opening opportunities for the realization of textiles with complex 3D shapes [29, 30]. Further, textiles are

© 2026 Wiley-VCH GmbH

flexible, compliant, and can provide protection from the elements [31], making them a natural material choice for wearable devices [32–34]. Textiles can be used as base materials onto which actuators, sensors, power supplies, and other discrete components are attached [35], but innovations in structuring, including weft-knitting, have led to textile-integrated actuators and sensors [36–41]. These devices are enabled by the fact that the mechanical properties of weft-knits are customizable across the surface [42–45]; however, it remains an open challenge to formalize rules that translate desired functionality into stitch-level design.

In this work, we leverage engineered mechanical instabilities to create functionality in textiles and demonstrate that weft knitting provides a platform to realize multistable textiles. We first introduce pronounced curvature into the knits as a function of stitch pattern. We then explore the relationship between the geometry – varied periodic stitch patterns – and mechanical properties – snap-through instabilities – of the knits.

We demonstrate that the curvature of knit textiles arises from pre-stresses introduced during manufacturing, since finite element simulations of bilayers with perpendicular internal stresses reproduce the curved shapes observed in the fabricated knits. We also investigate the variations in geometry, material, and machine parameters that result in multistability. Finally, we functionalize these multistable patterns by incorporating conductive elements to create soft switches with built-in haptic feedback. The unique combination of soft, breathable materials and snapping will enable reliable input and interaction with fully textile wearable devices. We envision these switches being integrated into cycling vests for increased visibility and communication while cycling in the dark, without distracting device operation. Users can also interact with and reconfigure a responsive soft structure.

2 | Knit Fabrics as Perpendicularly Pre-Stressed Bilayers

Similar to how a fused filament 3D printer transforms a 1D filament into a 3D structure, a knitting machine structures a 1D yarn into a 2D fabric (Figure 1A). This process occurs row by row, through the creation of interlocking slip knots on one of the two mirroring needle beds (Figure 1B). All our samples are realized using an automated double-bed weft-knitting machine (Kniterate) and an elastomeric nylon-spandex core-spun yarn (Yeoman Yarns). To visualize complex stitch patterns, we knit with four mechanically identical yarns in different colors (two blue and two orange) such that the face of the resulting fabric is orange and the reverse is blue (Figure 1B). All four yarns follow the same looped path, but the orange yarns are offset ahead (a process called plating), resulting in each side of the fabric displaying a different color. A jersey knit is the simplest of knit structures, where each knit stitch is an identical loop formed on one bed of the knitting machine.

We start by knitting a jersey fabric and cutting 5 cm × 20 cm samples aligned with the warp and weft directions (Figure 1C). All samples cut from this uniform fabric curl along all four edges, adopting a saddle shape. The sample with its length parallel to the warp direction curls along the long edge with the orange side facing outward (Figure 1D), while the sample with length parallel to the weft direction curls along the long edge with the blue side facing out (Figure 1E). The fact that the edges curl when cut demonstrates that internal stresses are present in the knit [24]. The observed curling mirrors that of a bilayer elastic sheet with perpendicular internal stresses [20, 22, 24, 25]. These internal stresses in the fabric result from the manufacturing process. In the knitting machine, tensile loads cause the yarn to stretch by 105% (Table S1). When released from the needles, the yarn contracts but cannot return to its original state due to the interlocked loop structure, retaining the tensile deformation as internal stress.

Examining the yarn paths further supports the analogy between the knits and a bilayer elastic sheet with perpendicular internal stresses; the yarns on the face of the fabric lie approximately parallel to the warp direction (Figure 1F; Figure S11), whereas on the reverse side the yarns lie approximately parallel to the weft direction (Figure 1G; Figure S11). We can therefore understand the fabric as a bilayer with the technical face and reverse side experiencing perpendicular compressive stresses along the warp and weft directions, respectively. An alternative mechanism has been proposed for the curvature of fabrics knitted from nearly inextensible yarns, such as wool, namely the relaxation of bending moments [29].

Until now, curvature in our samples is concentrated at the sample edges (Figure 1D–E; Figure S9). Pronounced curvatures within the bulk are introduced by knitting sections of a textile on the front and back beds of the machine [33, 36] (Figure 1B).

In particular, we start by knitting rib and garter (or links-links [46–48]) stitch patterns that consist of warp-direction (vertical) and weft-direction (horizontal) stripes, respectively, where each stripe is a column (rib) or row (garter) alternating between the front and back beds (front-knits and back-knits).

While the term 'links–links' is used to describe the broader category of stitch patterns that contain both front and back bed knits in a single column [46–48], here we refer to our set of horizontal and vertical striped patterns as garter $n \times n$ and rib $n \times n$, where n is the number of stitches in a front or back bed stripe [36]. In these striped fabrics, the internal stresses cause corrugations parallel to the stripes (Figures S13 and S14) which are visible in the cross-section (Figure 1H,I). Although both the rib and garter patterns are 12×12 (with each stripe 12 stitches wide) and exhibit corrugations, the shape of the knit stitch reflected in the front-knits and back-knits lead to different distributions of internal stresses that result in different curvature profiles (Figure 1H–I). These pronounced curvatures influence the mechanical response of the fabrics, which we characterize using an Instron tensile testing machine with boundaries fixed by hook grips, following the protocol described in Figure S3. The results show that the fabric is softer when pulled in the direction perpendicular to the stripes since the ridges must first unfold before the textile sheet itself begins to stretch (Figure 1H,I; Figure S14). In both directions, the response is smooth – there is no drop in force corresponding to snapping instabilities, – and reversible – the sample is monostable and returns to its initial configuration upon unloading.

16163028, 0, Downloaded from https://advanced.onlinelibrary.wiley.com/doi/10.1002/adfm.76385 by Harvard University, Wiley Online Library on [16/06/2026]. See the Terms and Conditions (https://onlinelibrary.wiley.com/terms-and-conditions) on Wiley Online Library for rules of use; OA articles are governed by the applicable Creative Commons License

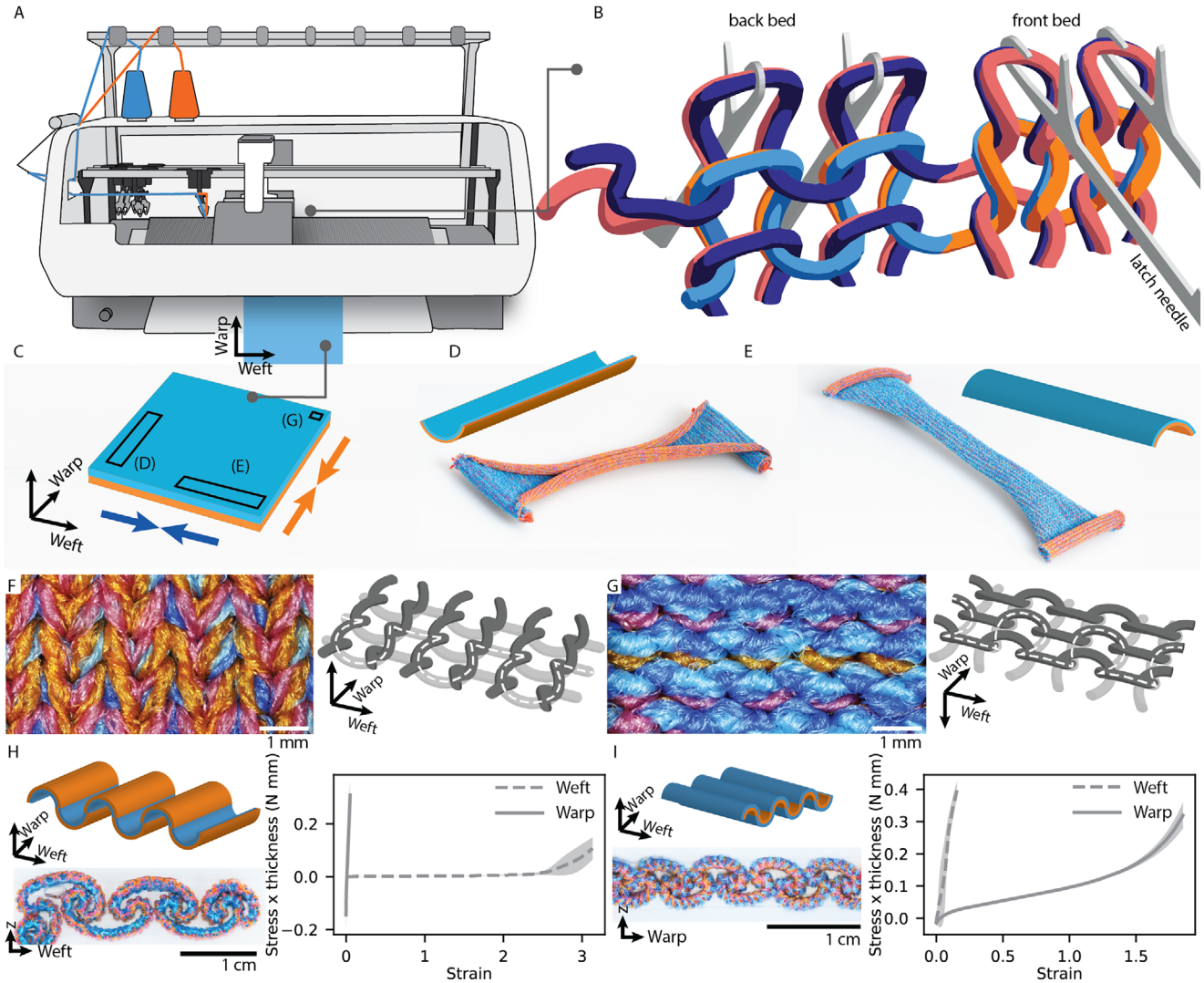


FIGURE 1 | Knitting on the front and back bed of a knitting machine allows us to create corrugated textiles. (A) The Kniterate machine. (B) Needles are arranged in two parallel beds facing each other. Colored yarns are held together in needles, but offset to color the two faces of the fabric in orange and blue. This needle configuration shows the rib structure in H. (C) A knit sample is approximated as a bilayer with perpendicular internal stresses. (D) A high aspect ratio sample is cut in the warp direction. A schematic shows the dominant curvature. (E) A high aspect ratio sample is cut in the weft direction, resulting in an opposing dominant curvature. (F) On the face of the fabric the yarns lie parallel to the warp direction, illustrated with a macro photograph with corresponding schematic. (G) On the reverse side the fabric yarns are parallel to the weft direction, shown via imaging and associated schematic. (H) Corrugations in the weft direction are known as a rib fabric. We visualize these corrugations by imaging the cross-section. This fabric is much more compliant in the weft direction as the vertical corrugations unfold. (I) Corrugations in the warp direction are known as a garter or links-links fabric. A cross-section image depicts the shape of the corrugations. In a tensile test, these corrugations cause this fabric to be compliant in the warp direction but stiff in the weft direction. All samples are knit on the Kniterate machine.

3 | Selective Patterning can Lead to Multistability

We harness internal stresses to generate pronounced local curvatures and exploit them for functionality. By selecting specific knit patterns of front-knits and back-knits, we engineer curved morphologies, snap-through instabilities, and multistability into the fabric. We consider unit cells composed of 4×4 blocks, with each block containing 12×12 stitches knit on either the front or back bed. There are 2^{16} possible unit cells that follow these rules, but we focus on three patterns that are balanced, i.e., they have an equal number of stitches knit on the front and back beds: a Step pattern (Figure 2A), a Windmill pattern (Figure 2B), and an H-shaped pattern (Figure 2C). By selecting patterns with the same number of stitches on the front bed and back bed, the local curvatures effectively cancel out, resulting in a fabric with no global curvature. We knit samples that are a 2×2 repeat of the unit cells, adding the first row once more at the end as handling regions to facilitate testing.

Upon manufacturing, all fabric samples exhibit pronounced natural curvature in the bulk (Figure 2D-i,E-i,F-i). When subject to point loading, all samples display J-shaped force-displacement curves (Figure 2G,H,I; Movie S1), with an initial low-stiffness region corresponding to unfolding, followed by a stiffening

16163028, 0, Downloaded from https://advanced.onlinelibrary.wiley.com/doi/10.1002/adfm.76385 by Harvard University, Wiley Online Library on [16/06/2026]. See the Terms and Conditions (https://onlinelibrary.wiley.com/terms-and-conditions) on Wiley Online Library for rules of use; OA articles are governed by the applicable Creative Commons License

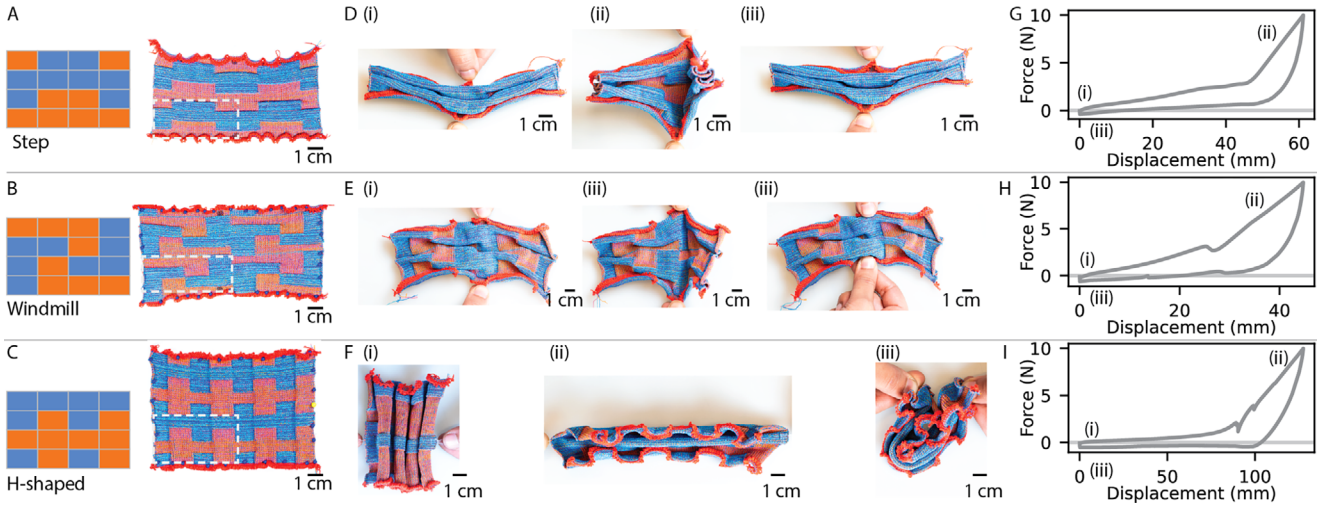


FIGURE 2 | By altering the unit cell knitting patterns we can tune both the final shape and mechanical response of the textile. (A) The Step pattern unit cell and corresponding knit sample. (B) The Windmill pattern unit cell and corresponding knit sample. (C) The H-shaped pattern and corresponding knit sample. (D) A Step sample (i) before loading, (ii) during loading, and (iii) after unloading. (E) A Windmill sample (i) before loading, (ii) during loading, and (iii) after unloading. (F) An H-shaped sample (i) before loading, (ii) during loading, and (iii) after unloading. (G–I) Force-displacement measurements for (G) the *Step* sample, (H) the Windmill sample, and (I) the H-shaped sample, with force drops marked and the region of negative force highlighted by a gray horizontal line. All samples are knit on the Kniterate machine.

regime associated with stretching [36, 49]. Samples also exhibit hysteresis due to internal friction between the yarns. Each pattern exhibits unique mechanical behavior, displayed in the force-displacement curves (Figure 2G,H,I) and snapshots taken at key points throughout the loading and unloading curves (Figure 2D,E,F).

In the Step pattern (Figure 2A), the horizontal garter stripes are perturbed, yet the distinctive horizontal folds remain (Figure 2D-i). When subjected to a local load by pulling two tabs, the recorded force-displacement curve is smooth, but a vertical fold appears close to the loading point (Figure 2D-ii), similar to the 'scars' seen in corrugated sheets [50]. In a uniform corrugated sheet, the fold is determined by only the location and direction of loading, whereas in our sample, the knitting pattern also affects the final configuration. The knit sample is therefore more robust to perturbations in the loading direction. The fabric returns to its initial configuration upon unloading (Figure 2D-iii). Additional photos and data are in Figure S15.

The Windmill pattern disrupts the continuous stripes, and non-perpendicular folds emerge (Figure 2E-i). Upon loading, the Windmill fabric exhibits a sudden drop in force (Figure 2H), a well-known phenomenon in elasticity which corresponds to a snapping instability [51, 52]. This snapping event results in the sudden formation of a vertical fold (Figure 2E-ii). During unloading, we observe a sudden increase in force, corresponding to a snap-back event, where the vertical fold disappears (Figure 2E-iii) and the fabric returns to its initial configuration. Additional photos and data are in Figure S16.

While the Step and Windmill patterns are monostable, patterned fabrics can also exhibit multistability [53]. To categorize a sample as multistable, we investigate the photographs of the textile before loading and after unloading, as shown in Figure 2F-i, iii. For a textile to be multistable, these two configurations must be different, as the shape of the textile has changed during loading. For the elastomeric yarns and machine settings in Figure 2, we also observe a sudden drop in force during loading, corresponding to a snap-through instability and transformation during loading.

An example of such multistable fabrics is the H-shaped pattern, which combines the vertical and horizontal stripes of the rib and garter stitches. This sample can fold in the warp, weft, or a combination of both directions, resulting in multiple stable states (Figure 2F). When the sample is loaded by pulling two tabs, two snapping events are triggered, each corresponding to the disappearance of a warp-direction fold and the appearance of a weft-direction fold (Figure 2I). While we cannot test all 2^{16} patterns, additional examples of both multistable and monostable patterns are shown in Figures S18 and S17. While Figure 2 presents results for samples subjected to point loads, multistability is also observed under different loading conditions. For instance, when the entire edge of a large H-shaped sample is pulled, the structure transitions into a secondary configuration (Figure S19). However, under these conditions, no snapping behavior is observed in the force–displacement curve, likely due to damping effects along the extended edge.

The unique curvature and mechanical response of these knits cannot be predicted from their flat configuration but are instead governed by the pre-stresses introduced during manufacturing. To demonstrate this, we conducted Finite Element simulations using the commercially available software (Abaqus 2021). In these simulations, the knits are modeled as continuum elastic bi-layer shells. Internal stresses originating from the knitting process are replicated in simulation by assigning mismatched orthogonal coefficients of thermal expansion ($\alpha_x = 0.165\ 1/C°$, $\alpha_y = 0.0198\ 1/C°$) to the two layers. The simulations consist of two steps; first, the temperature is increased, inducing internal stresses and curvature. Then we apply a point load to the model. In the layer representing the technical face of the fabric (shown

16163028, 0, Downloaded from https://advanced.onlinelibrary.wiley.com/doi/10.1002/adfm.76385 by Harvard University, Wiley Online Library on [16/06/2026]. See the Terms and Conditions (https://onlinelibrary.wiley.com/terms-and-conditions) on Wiley Online Library for rules of use; OA articles are governed by the applicable Creative Commons License

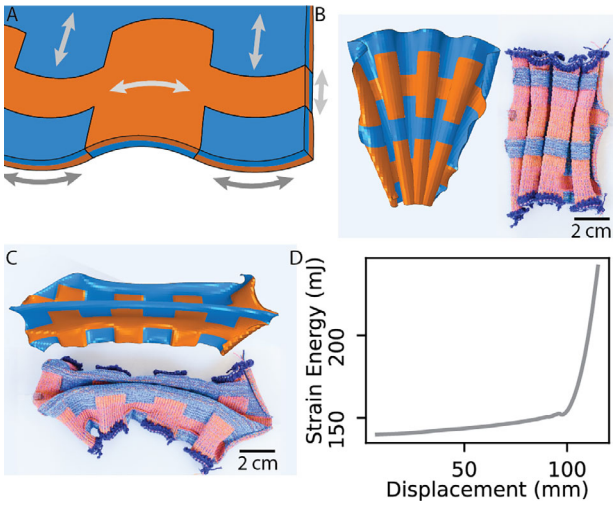


FIGURE 3 | Finite Element simulations demonstrate that the internal stresses in our knits resemble those of a perpendicularly pre-stressed bilayer. (A) Thermal expansion induces curvature and internal stresses in a bi-layer shell with mismatched orthogonal coefficients of thermal expansion. (B) This simplified representation of the fabrics is sufficient to achieve the curved configurations observed in experiments. (C) When a localized displacement is applied to the boundaries of the model, snapping into a second stable configuration is observed. (D) Numerically predicted evolution of the strain energy as a function of applied displacement exhibits two minima–one at zero displacement and another at a finite, nonzero displacement–confirming multistability.

in orange), the thermal expansion causes the layer to expand horizontally, whereas the layer representing the technical back of the fabric (shown in blue) expands vertically (Figure 3A). As shown in Figure 3B, this simplified representation of the fabrics is sufficient to achieve the curvature shown in experiments. In the second step, we apply a localized displacement to the curved model, mimicking the experimental loading conditions. The simulations reveal snapping and folding transitions corresponding to a secondary minimum in the system–s energy landscape (Figure 3C–D), confirming the textile's intrinsic multistability.

4 | Tuning Multistability

To investigate how universal this observed multistability is, we knit the H-shaped pattern on an alternate automated knitting machine (Shima Seiki SWG N2 15 gauge) and with varied yarns and stitch sizes. We select a 100% wool yarn (Peter Patchiss) and a yarn called 'fluid rayon' that is a blend of viscose, spandex, and nylon (Yeoman Yarns) in addition to the elastomeric nylon-spandex yarn we used previously. Each of these yarns are constructed differently, resulting in a different twist and surface texture (Figure 4A). In tensile tests of the yarn alone, we observe that the wool and viscose yarns break at higher forces and are much less extensible than the elastomeric yarns (Figure 4B). We knit these yarns using the same knit pattern as Figure 2C and compare the mechanical response. However, these yarns are also much thicker and have more loose radial fibers, so we use a larger stitch size to knit them, resulting in differing global shapes (Figure 4C). Despite the variation in surface, bending, and extensional properties of these yarns, all samples are multistable

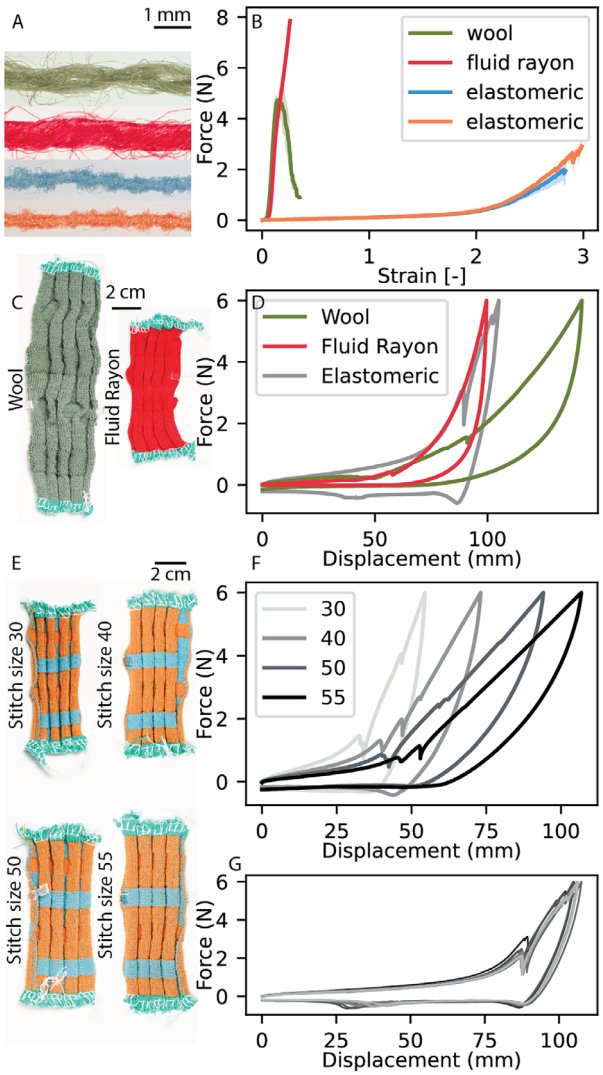


FIGURE 4 | (A) Microscope images of each of the yarns used. (B) Tensile tests of the yarns. (C) Images of the samples knit from alternate yarns (D) Tensile tests of the 'H-shape' knit pattern, knit with different yarns. (E) Photographs of samples knit with two elastomeric yarns on the Shima Seiki SWG machine in different stitch sizes (F) Tensile tests of the 'H-shape' knit pattern with different stitch sizes. (G) Repeated tensile tests of the sample from Figure 2C, knit with four ends of elastomeric yarn on the Kniterate machine.

and exhibit a steep drop in the force-displacement curve during loading, a signature of a snap-through instability (Figure 4D). Using two ends of elastomeric yarn (to accommodate the smaller gauge of the machine) and the same knitting pattern in Figures 2C and 4C, we sweep through the range of knittable loop sizes (30–55 in the machine units). As expected, we observe that scaling the stitch sizes leads to scaling the knitted sample (Figure 4E). However, despite the fact that the stiffnesses of the samples vary, for all of them we observe the existence of a force drop and, therefore, multistable behavior (Figure 4F). Finally, in order to test the repeatability of the response of our knits, we focus on the elastomeric sample tested in Figure 2C and repeat the same tensile test 10 times, resetting it manually after each test. As shown in Figure 4G, we find that the multistable response of the knits is reversible and repeatable.

16163028, 0, Downloaded from https://advanced.onlinelibrary.wiley.com/doi/10.1002/adfm.76385 by Harvard University, Wiley Online Library on [16/06/2026]. See the Terms and Conditions (https://onlinelibrary.wiley.com/terms-and-conditions) on Wiley Online Library for rules of use; OA articles are governed by the applicable Creative Commons License

Next, we control multistability by tuning the number of stitches in each block that is knit on either the front or back bed. We select the H-shaped pattern and vary the block size while maintaining rotational and reflective symmetries. Maintaining symmetries results in three geometric parameters (Figure S20). We vary the number of stitches for the width of the rib, n_a, for the height of the garter, n_b, and the height of the rib section, n_d (Figure 5A). Setting n_b or n_d to 0 recovers the rib and garter stitch patterns, respectively. We consider twenty-seven unique unit cells with n_a, n_b, and $n_d \in [4, 8, 12]$. The minimum size of four stitches was selected so that the curvature in the bulk of the samples remains larger than a single stitch. For each geometry, a sample of 2×2 unit cells was manufactured and point-loaded in the same way as shown in Figure 2. While geometric parameters can often be reduced to fewer non-dimensional numbers, we demonstrate that all three parameters, n_a, n_b, and n_d, affect the mechanical response separately.

For each of the twenty-seven samples, the force-displacement responses are shown in Figure 5B. Samples are characterized as monostable or multistable based on their shape before loading and after unloading, as shown in Figures S21, S22, and S23. Multistable samples are highlighted in purple, while monostable samples are color-coded based on the dominating folds in their stable configuration: yellow for the vertical folds and green for the horizontal folds (Figure 5C).

In this parameter space of twenty-seven geometries, we observe several trends (Figure 5D). Twelve of the samples we fabricate are monostable in the garter configuration, while two are monostable in the rib. This behavior is because we have selected a unit cell that is a combination of both stripes, but the horizontal garter stripes remain unbroken throughout, whereas the vertical rib stripes are interrupted. We only see the rib folds dominate when they have a small radius of curvature ($n_a = 4$), large area associated with the rib pattern ($n_d = 8$ or 12), and large radius of curvature in the garter direction ($n_b = 12$).

While it seems possible to reduce these parameters to non-dimensional numbers, the results indicate that multistability requires tuning n_a, n_b, and n_d together. For our geometry, setting parameters for the rib sections and garter sections are not equivalent. This could be due to the inherent anisotropic shape of the stitches themselves. The rib sections of the textile are defined by n_a, which sets the curvature of the rib folds, and n_d, which sets the height of the rib section. The garter section is defined by only one parameter, n_b, which sets the height of the horizontal stripe. This stripe height determines the curvature of this garter section. Therefore the curvature and height of the garter sections cannot be set independently. When n_b is large, the height of the garter section is large, but so is the radius of curvature, leading to less strong folds. As a result, although n_d/n_b defines the ratio between rib and garter stitches, it does not determine whether a fabric is monostable or bistable; samples with the same values of n_b and n_d do not demonstrate the same stability.

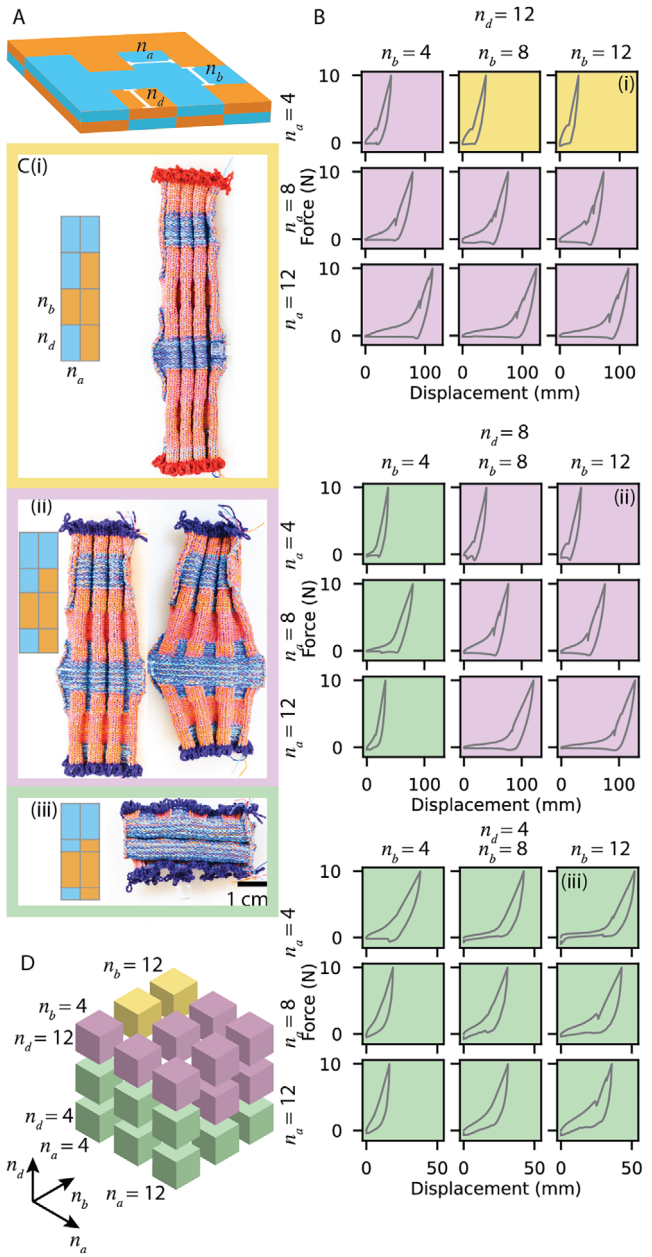


FIGURE 5 | As the geometric parameters of a single unit cell vary, so do the mechanical properties and 3D shapes of the textile. (A) Three parameters define our H-shaped unit cell (n_a, n_b, and n_d). Units of each parameter are number of stitches. (B) All three parameters are varied and the force-displacement response measured. Multistable samples are highlighted in purple, while monostable samples are color-coded based on the dominating folds in their stable configuration: yellow for the 'rib'–configuration and green for the 'garter'– configuration. Data for additional samples is available in Figures S24, S25, and S26. (C) Snapshots of samples with (i) $n_a = 4$, $n_b = 12$, and $n_d = 12$. (ii) $n_a = 4$, $n_b = 12$, and $n_d = 8$. (iii) $n_a = 4$, $n_b = 12$, and $n_d = 4$. Additional photos are shown in Figures S21, S22, and S23. (D) We visualize which samples are monostable rib - -yellow, – monostable garter - -green, – and bistable – purple – in the 3-D space of our parameters. All samples were knit on the Kniterate machine.

16163028, 0, Downloaded from https://advanced.onlinelibrary.wiley.com/doi/10.1002/adfm.76385 by Harvard University, Wiley Online Library on [16/06/2026]. See the Terms and Conditions (https://onlinelibrary.wiley.com/terms-and-conditions) on Wiley Online Library for rules of use; OA articles are governed by the applicable Creative Commons License

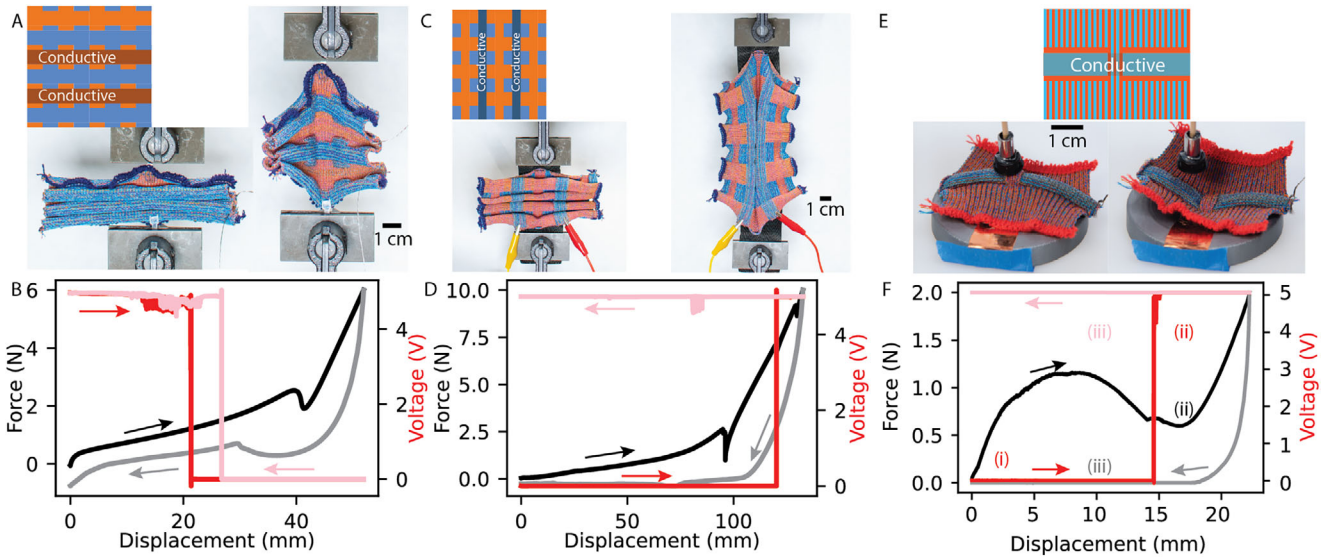


FIGURE 6 | By incorporating conductive ridges, we develop fully textile momentary and latch switches. (A) A monostable (momentary) switch consists of an H-shaped sample with $n_a = 8$, $n_b = 12$, and $n_d = 4$, and conductive yarn knit into two ridges. Upon stretching, these ridges are separated. (B) Voltage and force are both measured as a function of displacement. When the conductive ridges are in contact, the sensor measures 5V. (C) A multistable (latching) switch consists of an H-shaped sample with $n_a = 12$, $n_b = 12$, and $n_d = 12$, and conductive yarn knit into two ridges. This sample starts in the rib configuration. When both ridges have snapped into the garter configuration, they are in contact with each other. (D) Voltage and force are both measured as a function of displacement. (E) An out-of-plane multistable switch is made from the pattern of front and back bed knits that generates a domed button. When the fabric is indented, it snaps into a second stable configuration, and remains there when the load is removed. (F) Voltage and force are measured as a function of the indenter displacement. All samples were knit on the Kniterate machine.

5 | Functionality Through Conductive Elements

We harness both the snap-through behavior and the multistability of the fabric to build a momentary switch and latching switch with built-in haptic feedback.

While textile sensors allow for large amounts of scalar or vector data to be collected through unobtrusive means [54–57], our switches only transmit information about whether they are on or off. Input devices such as a keyboard do not require continuous measurement; a simple binary (on/off) response is beneficial due to less need for data or signal processing. Our devices also provide built-in haptic feedback when they snap between states, giving the user information about their state. In keyboards, light switches, and controls in cars, haptic feedback allows the user to interact with the built environment without direct visual cues [58]. Two key elements of our structure allow us to develop these switches with built-in haptic feedback. First, when a sample transforms from the 'rib' configuration to 'garter' configuration, the areas of self-contact change. By incorporating a conductive yarn (Figures S1 and S27) into the areas that make and break contact, we create a simple switch. Second, this transformation is marked by a steep drop in force which allows a user to know when contact is broken without a visual cue. Humans can sense forces as low as 10–100 mN; the force-drops we demonstrated are on the order of 0.1 N, and therefore detectable [59].

The momentary switch is realized using an H-shaped pattern with $n_a = 8$, $n_b = 12$, and $n_d = 4$, which exhibits snap-through instability but is monostable (Figure 5B). We add conductive yarn to the horizontal ridges that are in contact when the sample is unloaded (Figure 6A). We measure the voltage across this contact as a proxy for electrical conductivity as a function of applied displacement (Figure 6A). We observe that for an applied displacement of 20 mm the voltage drops to 0 since the contact between the initially horizontal ridges is broken. After contact is lost, a steep force drop occurs, letting the user know that the switch is on. Since this geometry is not multistable, we observe both a snap-back and the contact resuming upon unloading. A circuit composed of the textile switch in parallel with an LED (Figure S4) allows us to trigger lighting up of the LED when the contact within the textile is broken (Movie S2).

A latch switch stays on once activated until it is reconfigured, as do the multistable samples in Figure 5. We build a latch switch using an H-shaped pattern with $n_a = 12, n_b = 12$, and $n_d = 12$ that is multistable. The sample displays two force-drops which correspond to the formation of two horizontal ridges (Figure 6C). These two ridges have conductive yarn, and when they come into contact the voltage jumps to 5V. This contact occurs at a displacement between the two force drops; after the second force drop, the user knows the light is on (Figure 6D).

Until now, we focus on periodic geometries that snap under tension. However, our strategy can be generalized to non-periodic geometries. We demonstrate an example that behaves like a button, i.e., it snaps under a local compressive load and comes into contact with a plate below it. The button is designed to rise above a flat stitch pattern (1×1 rib - Figure 6E). A single stripe of garter interrupts this flat stitch, forming a ridge. Continuing the rib pattern through the center of the ridge transforms it into a button (Figure 6E-i). When pushed, this dome switches

16163028, 0, Downloaded from https://advanced.onlinelibrary.wiley.com/doi/10.1002/adfm.76385 by Harvard University, Wiley Online Library on [16/06/2026]. See the Terms and Conditions (https://onlinelibrary.wiley.com/terms-and-conditions) on Wiley Online Library for rules of use; OA articles are governed by the applicable Creative Commons License



FIGURE 7 | The momentary switch is further developed into a step counter and turn signaling sleeve for cycling. (A) The knit counter is attached to a sleeve by threads such that the opening and closing of the knee leads to the knit counter being point loaded. An attached Arduino microcontroller is able to count one full cycle of the counter opening and closing and display the total number of steps. (B) The whole device is shown to count one step when a user steps onto a stool. (C) The same knit textile is attached to the elbow joint, and is in the closed configuration when the elbow is flexed (i) and the open configuration when the elbow is extended (ii). (D) An attached circuit causes an LED arrow to switch on when the user signals to turn. (E) This device can be used to signal turns while cycling, allowing for increased visibility and safety. All samples were knit on the Kniterate machine.

to its inverted stable configuration and comes into contact with copper tape to complete the circuit (Figure 6E-ii,E-iii). This latch switch goes from "off" to "on" at the lowest point in the force-displacement curve, unlike the other two examples, and therefore the user can detect exactly when the switch turns on (Figure 6F; Movie S2).

A natural application for these textile switches is in wearable devices. By placing a momentary switch across the inside of a user's knee (Figure 7A), we can detect whether the knee is flexed (bent) or extended (straight). When the knee is flexed, the two conductive ridges come into contact with each other, and a circuit is closed. When the knee is extended, this circuit remains open. An Arduino microcontroller records each cycle of closing and opening as a step, and the total number of steps is displayed on the built in display (Figure 7B). The knit piece here acts as a binary sensor which simplifies the complex motion involved in a step into a simple cycle of "on" and "off" (Movie S3).

In addition to this lower limb device, we also place the momentary switch across the elbow joint in order to detect whether the elbow is flexed or extended. The ridges are in contact while the user's elbow is bent and contact is broken when the user's arm is straight (Figure 7C). The switch is incorporated into a sleeve along with a series of lights that display an arrow when the arm is straight (Movie S3). This allows the user to signal a turn while increasing visibility during cycling at night.

The user can communicate using the existing hand signal for turning while cycling, and the snapping behavior of the switch allows the user to feel whether the light is on or off without visual feedback or confirmation. Analogous to haptic feedback

16163028, 0, Downloaded from https://advanced.onlinelibrary.wiley.com/doi/10.1002/adfm.76385 by Harvard University, Wiley Online Library on [16/06/2026]. See the Terms and Conditions (https://onlinelibrary.wiley.com/terms-and-conditions) on Wiley Online Library for rules of use; OA articles are governed by the applicable Creative Commons License

in car buttons and switches, this allows the cyclist to focus their eyes and ears on the road since the device inputs through the sense of touch. The whole device remains soft and breathable, important characteristics for a garment that will be worn during high output exercise.

This device provides haptic feedback while allowing a cyclist to use established hand signals.

While popular in wearables, textiles are also found in household items and furnishings. They are easy to clean, comfortable, and diffuse light in lamps and window coverings. With this in mind, we develop an adaptable textile lamp in which multistability enables shape reconfiguration and serves as an electronic latch switch. To form this lamp, we sew a rectangular panel of three parallel latch switches into a cylinder.

These panels were all knit on the Shima Seiki SWG machine for larger size and increased reliability. Each switch consists of two rings that come into contact with each other. An LED is placed in parallel with each switch so that the light shines when the switch is open. In Figure 8A, all three switches are closed, and the lights are off. Any of the eight combinations of three LEDs are possible – we demonstrate three in Figure 8B–D. The entire textile is multistable, and the switches wrap around the whole cylinder, allowing this lamp to be reconfigured into any shape and combination of "on" lights (Figure 8E; Movie S4). As the structure changes shape, individual unit cells snap back and forth, providing haptic feedback that help the user to understand how the lighting will respond. This textile lamp is also lightweight and portable, weighing 71.4g including all electronics and fits into a single hand. Designed and knit on an industrial machine, the textile portion of this lamp takes 25 min to knit and is scalable, paving the way for interactive, morphing textiles for the home.

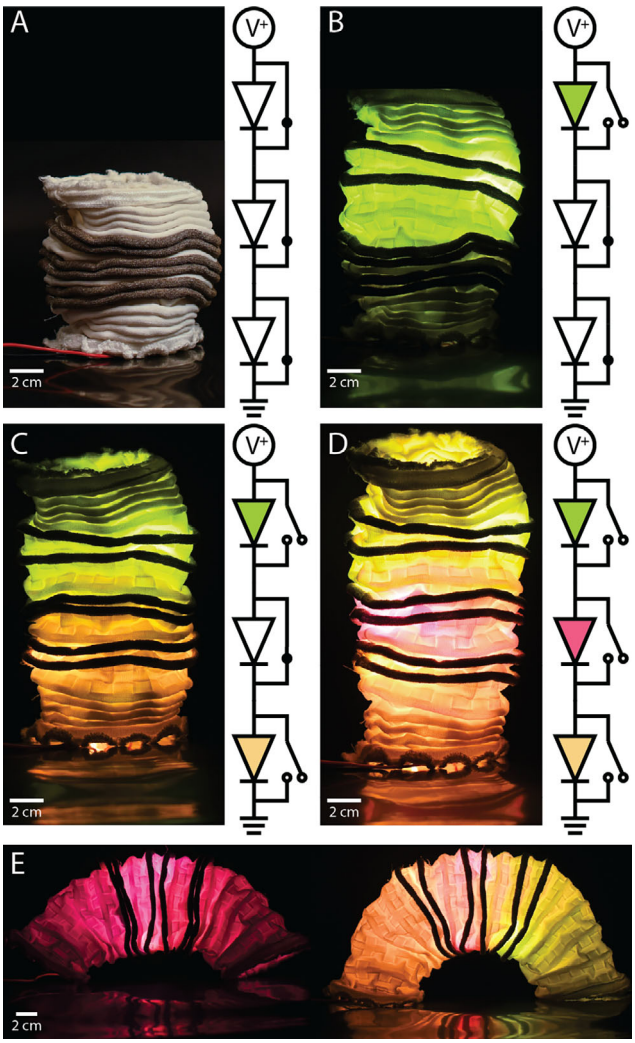


FIGURE 8 | We combine three latch switches to create a reconfigurable lamp. (A) The lamp is off. All three switches are closed. (B) One, (C) two, and (D) three switches are open, corresponding to one, two, and three LEDs switching on. (E) The multistability of the structure allows a user to reconfigure the switches and the global shape. All samples were knit on the Shima Seiki SWG machine.

6 | Conclusion

To summarize, we have presented a perspective on modeling the curvature of a knit structure as a perpendicularly pre-stressed bilayer. This approach allows for the creation of complex curved knit surfaces that exhibit snap-through instabilities and multistability.

In the future, a more detailed investigation into the interactions and stresses in the individual yarns would allow for the creation of an analytical continuum model of these textiles. We demonstrated that the onset of multistability can be tuned by altering both the shape and dimensions of the knit patterns, and that this multistability is robust across materials and knitting parameters. Furthermore, functionality is added by incorporating conductive areas, enabling the design of momentary and latch switches with built-in haptic feedback. These switches open avenues for soft wearable devices that users can interact with without the need for external motors or visual feedback. With the advent of 'the internet of things,' engineers and artists are searching for new ways to interact with the natural and built worlds, and these lightweight, breathable, and compliant switches can be integrated into garments and wearable robots without additional bulk or weight. We have demonstrated a switch across both the elbow and knee joints. These switches can be adapted to be triggered in response to an uneven gait or terrain to provide feedback to controllers in assistive devices that provide additional support or stabilization. Wearables are not the only textiles we interact with on a daily basis; we also demonstrate an interactive textile lamp which can be reconfigured to produce different lighting effects and shapes. These haptic interfaces can also be incorporated into upholstered interiors, including cars and furniture.

While this study explores only a small portion of the vast design space of knit patterns, future work can build on this framework by extending our Finite Element model to predict the exact curvature and mechanical properties of a broader range of knit patterns, enabling the creation of a new class of functional and wearable devices.

16163028, 0, Downloaded from https://advanced.onlinelibrary.wiley.com/doi/10.1002/adfm.76385 by Harvard University, Wiley Online Library on [16/06/2026]. See the Terms and Conditions (https://onlinelibrary.wiley.com/terms-and-conditions) on Wiley Online Library for rules of use; OA articles are governed by the applicable Creative Commons License

7 | Methods

All knit samples were fabricated on either a Kniterate knitting machine or a Shima Seiki SWG N2 061 using knitout, a Python frontend, and Kniterate backend [60–62]. The details of the materials and fabrication methods are further summarized in Sections S1 and S2. The experimental procedure of the tensile testing of textile samples are in Section S3. The details of the Finite Element simulations are in the GitHub repository For reference, all relevant codes are available in the accompanying GitHub repository (https://github.com/bertoldi-collab/multistableknits_FE). Finally, additional data showing repeated experiments and additional knit patterns are shown in Section S4.

Acknowledgments

Research was supported by the NSF grant DMR-2011754 and ARO MURI program W911NF-22-1-0219. Equipment was supported by ONR DURIP Award N00014-19-1-2220. K.B. also acknowledges support from the Simons Collaboration on Extreme Wave Phenomena Based on Symmetries. V.S. also acknowledges salary support from NSF grant DMR-2138020 for the MPS-Ascend program. The authors would like to thank the Carnegie Mellon Textiles Lab and Prof. Jim McCann for discussions and resources relating to machine knitting. They also thank Dr. Anne Meeussen, Helen E. Read, Prof. Ahmad Rafsanjani, and Prof. Antonio E. Forte for insightful conversations and feedback.

Conflicts of Interest

The authors declare no conflicts of interest.

Data Availability Statement

The data that support the findings of this study are openly available in github at https://github.com/bertoldi-collab/multistableknits_FE.

References

1. B. Audoly and Y. Pomeau, "Elasticity and Geometry," in *Peyresq Lectures on Nonlinear Phenomena* (World Scientific, 2000), 1–35.

2. S. Timoshenko and S. Woinowsky-Krieger, *Theory of Plates and Shells*, 2nd ed. (McGraw-Hill, New York, 1959).

3. J. W. Hutchinson, "EML Webinar Overview: New Developments in Shell Stability," *Extreme Mechanics Letters* 39 (2020): 100805.

4. B. Camescasse, A. Fernandes, and J. Pouget, "Bistable Buckled Beam and Force Actuation: Experimental Validations," *International Journal of Solids and Structures* 51, no. 9 (2014): 1750–1757.

5. S. Poincloux, C. Vallat, T. Chen, T. G. Sano, and P. M. Reis, "Indentation and Stability of Woven Domes," *Extreme Mechanics Letters* 59 (2023): 101968.

6. W. Huang, Z. Liu, M. Liu, and K. J. Hsia, "Snap-Through Eversion of Axisymmetric Shells Under Contact Indentation," *Proceedings of the Royal Society A: Mathematical, Physical and Engineering Sciences* 480, no. 2300 (2024): 20240068.

7. P. M. Reis, "A Perspective on the Revival of Structural (In)Stability with Novel Opportunities for Function: From Buckliphobia to Buckliphilia," *Journal of Applied Mechanics* 82, no. 11 (2015): 111001.

8. M. Koh, Y. Wang, K. Shea, and T. Chen, "Shape Reconfiguring Bistable Structures Using Heat-Activated Fibers," *Engineering Structures* 295 (2023): 116792.

9. B. Gorissen, D. Melancon, N. Vasios, M. Torbati, and K. Bertoldi, "Inflatable Soft Jumper Inspired by Shell Snapping," *Science Robotics* 5, no. 42 (2020): eabb1967.

10. A. Djellouli, P. Marmottant, H. Djeridi, C. Quilliet, and G. Coupier, "Buckling Instability Causes Inertial Thrust for Spherical Swimmers at All Scales," *Physical Review Letters* 119, no. 22 (2017): 224501.

11. W. K. Lee, D. J. Preston, M. P. Nemitz, et al., "A Buckling-Sheet Ring Oscillator for Electronics-Free, Multimodal Locomotion," *Science Robotics* 7, no. 63 (2022): eabg5812.

12. T. Chen, O. R. Bilal, K. Shea, and C. Daraio, "Harnessing Bistability for Directional Propulsion of Soft, Untethered Robots," *Proceedings of the National Academy of Sciences* 115, no. 22 (2018): 5698–5702.

13. A. Djellouli, B. Van Raemdonck, Y. Wang, et al., "Shell Buckling for Programmable Metafluids," *Nature* 635, no. 8039 (2024): 565–571.

14. M. Gomez, D. E. Moulton, and D. Vella, "Passive Control of Viscous Flow via Elastic Snap-Through," *Physical Review Letters* 119, no. 14 (2017): 144502.

15. D. P. Holmes and A. J. Crosby, "Snapping Surfaces," *Advanced Materials* 19, no. 21 (2007): 3589–3593.

16. P. Rothemund, A. Ainla, L. Belding, et al., "A Soft, Bistable Valve for Autonomous Control of Soft Actuators," *Science Robotics* 3, no. 16 (2018): eaar7986.

17. N. Nadkarni, A. F. Arrieta, C. Chong, D. M. Kochmann, and C. Daraio, "Unidirectional Transition Waves in Bistable Lattices," *Physical Review Letters* 116, no. 24 (2016): 244501.

18. A. Lee, P. T. Brun, J. Marthelot, G. Balestra, F. Gallaire, and P. M. Reis, "Fabrication of Slender Elastic Shells by the Coating of Curved Surfaces," *Nature Communications* 7, no. 1 (2016): 11155.

19. T. J. Jones, E. Jambon-Puillet, J. Marthelot, and P. T. Brun, "Bubble Casting Soft Robotics," *Nature* 599, no. 7884 (2021): 229–233.

20. M. Pezzulla, G. P. Smith, P. Nardinocchi, and D. P. Holmes, "Geometry and Mechanics of Thin Growing Bilayers," *Soft Matter* 12, no. 19 (2016): 4435–4442.

21. Y. Klein, E. Efrati, and E. Sharon, "Shaping of Elastic Sheets by Prescription of Non-Euclidean Metrics," *Science* 315, no. 5815 (2007): 1116–1120.

22. M. Pezzulla, S. A. Shillig, P. Nardinocchi, and D. P. Holmes, "Morphing of Geometric Composites via Residual Swelling," *Soft Matter* 11, no. 29 (2015): 5812–5820.

23. P. Nardinocchi, M. Pezzulla, and L. Teresi, "Anisotropic Swelling of Thin Gel Sheets," *Soft Matter* 11, no. 8 (2015): 1492–1499.

24. S. Armon, E. Efrati, R. Kupferman, and E. Sharon, "Geometry and Mechanics in the Opening of Chiral Seed Pods," *Science* 333, no. 6050 (2011): 1726–1730.

25. Z. Chen, Q. Guo, C. Majidi, W. Chen, D. J. Srolovitz, and M. P. Haataja, "Nonlinear Geometric Effects in Mechanical Bistable Morphing Structures," *Physical Review Letters* 109, no. 11 (2012): 114302.

26. K. A. Seffen and S. D. Guest, "Prestressed Morphing Bistable and Neutrally Stable Shells," *Journal of Applied Mechanics* 78, no. 1 (2011): 011002.

27. Q. Guo, A. K. Mehta, M. A. Grover, W. Chen, D. G. Lynn, and Z. Chen, "Shape Selection and Multi-Stability in Helical Ribbons," *Applied Physics Letters* 104, no. 21 (2014): 211901.

28. K. Singal, M. S. Dimitriyev, S. E. Gonzalez, A. P. Cachine, S. Quinn, and E. A. Matsumoto, "Programming Mechanics in Knitted Materials, Stitch by Stitch," *Nature Communications* 15, no. 1 (2024): 2622.

29. L. Niu, G. Dion, and R. D. Kamien, "Geometric Modeling of Knitted Fabrics," *Proceedings of the National Academy of Sciences* 122, no. 7 (2025): e2416536122.

16163028, 0, Downloaded from https://advanced.onlinelibrary.wiley.com/doi/10.1002/adfm.76385 by Harvard University, Wiley Online Library on [16/06/2026]. See the Terms and Conditions (https://onlinelibrary.wiley.com/terms-and-conditions) on Wiley Online Library for rules of use; OA articles are governed by the applicable Creative Commons License

30. K. Tajiri, R. Murakami, S. Kobayashi, R. Tarumi, and T. G. Sano, "Curling Morphology of Knitted Fabrics: Structure and Mechanics," *Extreme Mechanics Letters* 76 (2025): 102300.

31. V. Sanchez, C. J. Walsh, and R. J. Wood, "Textile Technology for Soft Robotic and Autonomous Garments," *Advanced Functional Materials* 31, no. 6 (2021): 2008278.

32. K. Mahadevan, A. Stoltzfus, S. Dealey, and R. Granberry, "3D Knit Pneumatic Actuators for Wearable Haptic Displays," *Extreme Mechanics Letters* 65 (2023): 102102.

33. J. Abel, J. Luntz, and D. Brei, "Hierarchical Architecture of Active Knits," *Smart Materials and Structures* 22, no. 12 (2013): 125001.

34. C. T. O'Neill, C. M. McCann, C. J. Hohimer, K. Bertoldi, and C. J. Walsh, "Unfolding Textile-Based Pneumatic Actuators for Wearable Applications," *Soft Robotics* 9, no. 1 (2022): 163–172.

35. K. L. Dorsey, S. F. Roberts, J. Forman, and H. Ishii, "Analysis of Defextiles: A 3D-Printed Textile Towards Garments and Accessories," *Journal of Micromechanics and Microengineering* 32, no. 3 (2022): 034005.

36. V. Sanchez, K. Mahadevan, G. Ohlson, et al., "3D Knitting for Pneumatic Soft Robotics," *Advanced Functional Materials* 33, no. 20 (2023): 2212541.

37. Y. Luo, K. Wu, A. Spielberg, et al., "Digital Fabrication of Pneumatic Actuators with Integrated Sensing by Machine Knitting," in *Proceedings of the 2022 CHI Conference on Human Factors in Computing Systems* (2022): 1–13.

38. L. Albaugh, S. Hudson, and L. Yao, "Digital Fabrication of Soft Actuated Objects by Machine Knitting," in *Proceedings of the 2019 CHI Conference on Human Factors in Computing Systems* (2019): 1–13.

39. R. Granberry, K. Eschen, B. Holschuh, and J. Abel, "Functionally Graded Knitted Actuators with NiTi-Based Shape Memory Alloys for Topographically Self-Fitting Wearables," *Advanced Materials Technologies* 4, no. 11 (2019): 1900548.

40. O. A. Araromi, M. A. Graule, K. L. Dorsey, et al., "Ultra-Sensitive and Resilient Compliant Strain Gauges for Soft Machines," *Nature* 587, no. 7833 (2020): 219–224.

41. C. du Pasquier, L. Tessmer, I. Scholl, et al., "HaptiKnit: Distributed Stiffness Knitting for Wearable Haptics," *Science Robotics* 9, no. 97 (2024): eado3887.

42. H. Jayamaha, K. Park, and L. M. Shepherd, "Ultrablack Wool Textiles Inspired by Hierarchical Avian Structure," *Nature Communications* 16, no. 1 (2025): 10581.

43. M. Hofmann, L. Albaugh, T. Wang, J. Mankoff, and S. E. Hudson, "KnitScript: A Domain-Specific Scripting Language for Advanced Machine Knitting," in *Proceedings of the 36th Annual ACM Symposium on User Interface Software and Technology* (2023): 1–21.

44. C. du Pasquier, S. Jeong, P. Liu, et al., "Multi-Level Mechanical Modeling and Computational Design Framework for Weft Knitted Fabrics," *Extreme Mechanics Letters* 79 (2025): 102423.

45. B. Cline, C. Bai, S. Jeong, et al., "Entanglement-Driven Responses Through Multiscale 3D-Printed Knits," *arXiv Preprint arXiv:2511.07404* (2025).

46. D. Rant, R. Cıobanu, M. Blaga, and A. Pavko-Cuden, "Compression of Foldable Links-Links Knitted Structures," *Textile and Apparel* 24, no. 4 (2014): 349–355.

47. R. Tung, P. Yip, and J. Kwan, *The Knitwear Manual* (Fashionary International, Kowloon, Hong Kong, Nov. 2024).

48. F. Tellier-Loumagne, *The Art of Knitting: Inspirational Stitches, Textures, and Surfaces* (Thames & Hudson, London, England, June 2005).

49. C. Amanatides, O. Ghita, K. E. Evans, and G. Dion, "Characterizing and Predicting the Self-Folding Behavior of Weft-Knit Fabrics," *Textile Research Journal* 92, no. 21–22 (2022): 4060–4076.

50. A. Meeussen and M. van Hecke, "Multistable Sheets with Rewritable Patterns for Switchable Shape-Morphing," *Nature* 621, no. 7979 (2023): 516–520.

51. S. Timoshenko and J. Gere, *Theory of Elastic Stability*, 2nd ed. (McGraw-Hill, 1961).

52. Z. P. Bažant and L. Cedolin, *Stability of Structures: Elastic, Inelastic, Fracture and Damage Theories* (Oxford University Press, 1991).

53. S. Ahlquist, "Exploration of Multi-Stable Rib-Knit Textiles," https://vimeo.com/125186203 (2015).

54. A. Chaudhari, R. Lokesh, V. Chheang, et al., "Characterizing the Sensing Response of Carbon Nanocomposite-Based Wearable Sensors on Elbow Joint Using an End Point Robot and Virtual Reality," *Sensors* 24, no. 15 (2024): 4894.

55. Q. Chen, D. Xu, Y. Yan, et al., "A Self-Powered Tennis Training System Based on Micro-Nano Structured Sensing Yarn Arrays," *Advanced Functional Materials* 35, no. 5 (2025): 2414395.

56. G. Hang, Z. Liu, Y. Fu, J. Cao, X. Wu, and X. Wang, "Multidimensional Bionic Structure-Based Superhydrophobic and Stretchable Yarn Sensor for Motion Monitoring," *ACS Applied Nano Materials* 8, no. 5 (2025): 2432–2442.

57. X. Cheng, D. Shen, K. Zheng, Z. Wu, L. Shi, and X. Hu, "A Wearable Strain Sensor for Medical Rehabilitation Based on Piezoresistive Knitting Textile," *Sensors and Actuators A: Physical* 387 (2025): 116379.

58. H. Culbertson, S. B. Schorr, and A. M. Okamura, "Haptics: The Present and Future of Artificial Touch Sensation," *Annual Review of Control, Robotics, and Autonomous Systems* 1, no. 1 (2018): 385–409.

59. J. Yin, R. Hinchet, H. Shea, and C. Majidi, "Wearable Soft Technologies for Haptic Sensing and Feedback," *Advanced Functional Materials* 31, no. 39 (2021): 2007428.

60. J. McCann, L. Albaugh, V. Narayanan, et al., "A Compiler for 3D Machine Knitting," *ACM Transactions on Graphics (TOG)* 35, no. 4 (2016): 1–11.

61. V. Narayanan and J. McCann, "Knitout-Frontend-Py," https://github.com/textiles-lab/knitout-frontend-py (2021).

62. V. Narayanan, G. Ohlson, and J. McCann, "Knitout-to-Kcode Backend," https://github.com/textiles-lab/knitout-backend-kniterate (2021).

Supporting Information

Additional supporting information can be found online in the Supporting Information section.

Supporting File 1: adfm76385-sup-0001-SuppMat.pdf.

Supporting Movie 2: adfm76385-sup-0002-MovieS1.mp4.

Supporting Movie 3: adfm76385-sup-0003-MovieS2.mp4.

Supporting Movie 4: adfm76385-sup-0004-MovieS3.mp4.

Supporting Movie 5: adfm76385-sup-0005-MovieS4.mp4.

16163028, 0, Downloaded from https://advanced.onlinelibrary.wiley.com/doi/10.1002/adfm.76385 by Harvard University, Wiley Online Library on [16/06/2026]. See the Terms and Conditions (https://onlinelibrary.wiley.com/terms-and-conditions) on Wiley Online Library for rules of use; OA articles are governed by the applicable Creative Commons License

Supporting Information for: Knitting Multistability

Kausalya Mahadevan[1] Michelle C. Yuen[1,2] David T. Farrell[1] Conor J. Walsh[1]

Vanessa Sanchez,[1,3] Robert J. Wood,[1] Katia Bertoldi[1]

[1] John A. Paulson School of Engineering and Applied Sciences, Harvard University, 29 Oxford St., Cambridge, MA 02138, USA

[2] Department of Mechanical & Industrial Engineering, Montana State University, 220 Roberts Hall, Bozeman, MT 59717, USA

[3] Department of Mechanical Engineering, Rice University, 6100 Main St, Houston, TX 77005, USA

S1 Materials

Elastomeric Yarns: Elastomeric yarn samples were produced using four ends of Yeoman Yarns Elastomeric Nylon Lycra (Yeoman Yarns, United Kingdom), made from 81% nylon and 19% Lycra (a brand name of spandex), and plated together (i.e., knit together as one yarn).

Conductive Yarn: Two ends of conductive yarn were added to the existing four ends of elastomeric yarn in order to create conductive sections of textile. The conductive yarn used is '20 dtex Lycra + 44Ag + 44 roh Twisted Yarn', purchased from V Technical Textiles, Palmyra, NY.

Fluid Rayon: The fluid rayon yarn used has a composition of 2% Elastane, 7% Nylon, and 91% Viscose. It is a single-ply yarn purchased from Yeoman Yarns, United Kingdom. Samples knit in this work from this yarn used one end of yarn and did not undergo any postprocessing.

Wool: The wool yarn used here is 100 % wool. It is a two-ply yarn purchased from Peter Patchiss Yarns, Rhode Island, USA. Samples knit in this work from this yarn used one end of yarn and did not undergo any postprocessing.

Acrylic Waste Yarn: Three rows of acrylic yarn (16/2 Vybralite Acrylic Yarns, National Spinning Co. (Peter Patchis Yarns, USA)) were knit to start and end each sample to facilitate fabrication and prevent unraveling.

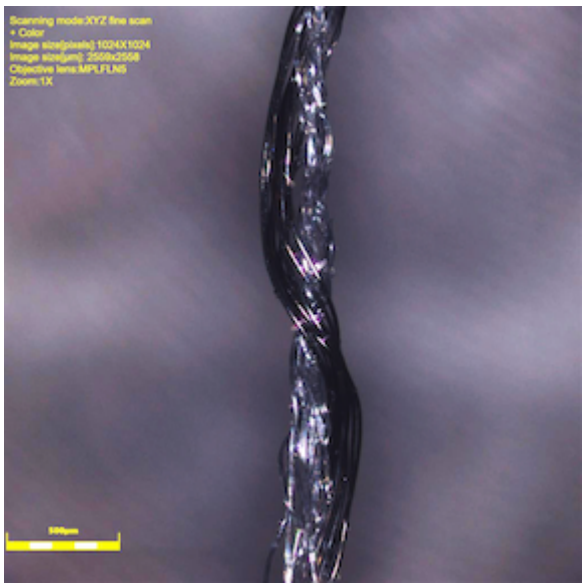


Figure S1: A microscope image shows the conductive fibers twisted around a Lycra core. Scale bar is 500 μm.

S2 Fabrication

Automated knitting

All samples were knit on the Kniterate knitting machine with stitch size 5 and four ends of elastomeric yarn fed as one. Conductive areas of textile were fabricated by threading a separate feeder with four ends of elastomeric yarn and two ends of conductive yarn. This feeder was used to knit the rows required to be conductive.

Through a series of springs, the yarn fed into the Kniterate machine is held under tension. We approximate the strain applied by the machine as follows: While under tension in the machine, five sections of each yarn 10 cm in length are measured and cut, which releases the tension [1]. The relaxed length of these yarn sections is then measured with a ruler and the tensile strain calculated by

$$\varepsilon = \frac{10 - l_0}{l_0}, \tag{S1}$$

where l_0 is the measured length (in centimeters) of each yarn section once the tension is removed. The tensile strains are reported in Table S1. The average strain across all colors and sections is 1.05.

Each stitch pattern shown was defined by a grid of black and white squares in Adobe Photoshop. These images were then read into python, where they were converted into knitout code using the python frontend [2]. The resulting knitout files were then compiled to '.kc' files through the knitout-to-kniterate backend [3], which are the format required by the kniterate machine. Three rows of acrylic waste yarn were knit onto the start and end of each sample for ease of knitting as well as for handling purposes (e.g., to prevent unraveling of the samples' testing region).

Table S1: Strain approximation of the yarn in the machine. Five 10 cm linear tracts of each yarn are cut while under tension in the machine. The relaxed length of these yarn sections is then measured with a ruler and the tensile strain calculated as in Equation S1. The average across all colors and sections is 1.05

	Orange 1	**Orange 2**	**Blue 1**	**Blue 2**
Tensile strain imposed by knitting machine [mm / mm]	1.63	1.17	0.89	0.79
	1.56	1.04	0.85	0.82
	1.56	1.08	0.82	0.85
	1.50	1.08	0.82	0.82
	1.33	0.92	0.67	0.89
Mean	1.52	1.06	0.81	0.83
Std Dev	0.12	0.09	0.08	0.04

Device fabrication

Turn-signal wearable device. The turn-signal wearable device described in Fig. 7 of the main text was fabricated onto a base of a cooling compression sleeve with a thumbhole made from 4-way stretch fabric (Teveuni, China). The sleeve was cut open to assemble the device. Dragonskin 10 was applied in a thin layer on the inside of the sleeve on either side of the elbow joint to anchor the sleeve to the wearer and provide better force transfer between the knit sample and the wearer (Fig. S2). A flexible LED filament (Adafruit) was connected via wire and conductive thread to the textile switch, which was hand-sewn across the elbow joint. After the circuit was assembled, the sleeve was stitched back into a tube on a five-thread overlock machine. This device can be powered by either a desktop power supply or portable USB-C power bank, which can weigh as little as 250g.

Lamp. The knit portion of the lamp described in Fig. 8 of the main text was fabricated by knitting a bistable substrate with three paired bands of conductive textile, where each serves as one of three switches. These three switches were each individually paired with a commercially available flexible LED filament in parallel, and then each switch-LED pair was connected in series. When each switch was closed, its corresponding LED filament would turn off as the current would pass through the switch; when each switch opened, its LED filament would illuminate. The circuit was powered with a DC power supply set at 7.5V and current-limited at 0.04A.

Step counter. The step counter device described in Fig. 7 was fabricated using a base of a Spandex fabric tube, which was then instrumented with a monostable knit sample attached spanning the inside of the knee joint. The two conductive regions of the knit sample form a switch that would repeatedly make and break contact with each step. This switch state was monitored with a digital input pin on an Arduino Nano Every, with the step count being incremented each time the switch closed during knee bending. This device is powered by a portable USB-C power bank, which can weigh as little as 250g and fits into a pocket.



Figure S2: The inside of the turn-signal sleeve during the fabrication process shows the silicone (DragonSkin 10, Smooth-On) coating before addition of circuitry and re-assembly.

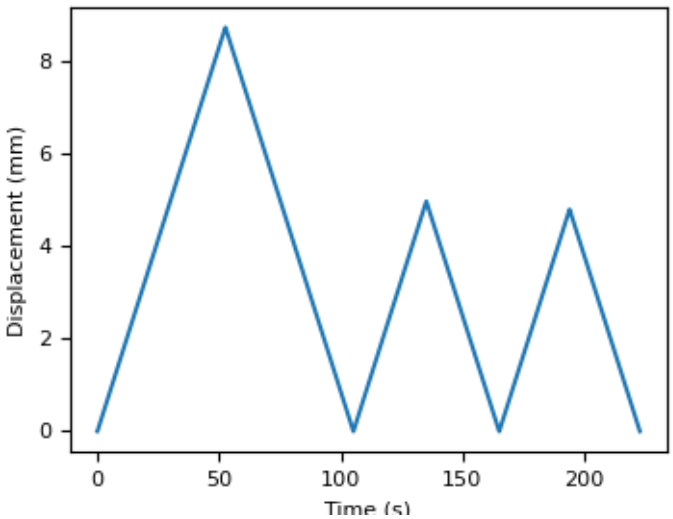


Figure S3: An example of the displacement-controlled protocol for tensile testing of rib, garter, and jersey samples. The first cycle's peak is at 25 N, and the second and third cycle's peaks are at 15N. The second cycle of multiple samples is averaged and presented in Figures 2, S13, S14, S10

.

S3 Testing

Rib, garter, and jersey samples were tested on an Instron tensile testing machine with boundaries fixed by a set of hook grips previously described [4]. Samples with complex curvature are point-loaded in order to isolate and observe local deformation defining multistability. Point loading is accomplished by gluing a 5mm x 15 mm acrylic tab to each sample using Loctite 416 instant adhesive. The stiff acrylic tabs allow force to be transferred from the textile sample back to the load cell, allowing us to measure negative forces.

All samples are loaded and unloaded at 10 mm/min. The rib, garter and jersey samples are cycled three times, up to 25N, 15N , and 15 N (Fig. S3). The samples with complex geometry (i.e., *Step*, *Windmill*, *H-shaped*) are loaded through a single cycle up to 10N.

For samples where voltage is measured, a circuit connects the sample to a power source and the Instron tensile tester, enabling synchronized recording of voltage, force, and displacement (Fig. S4).

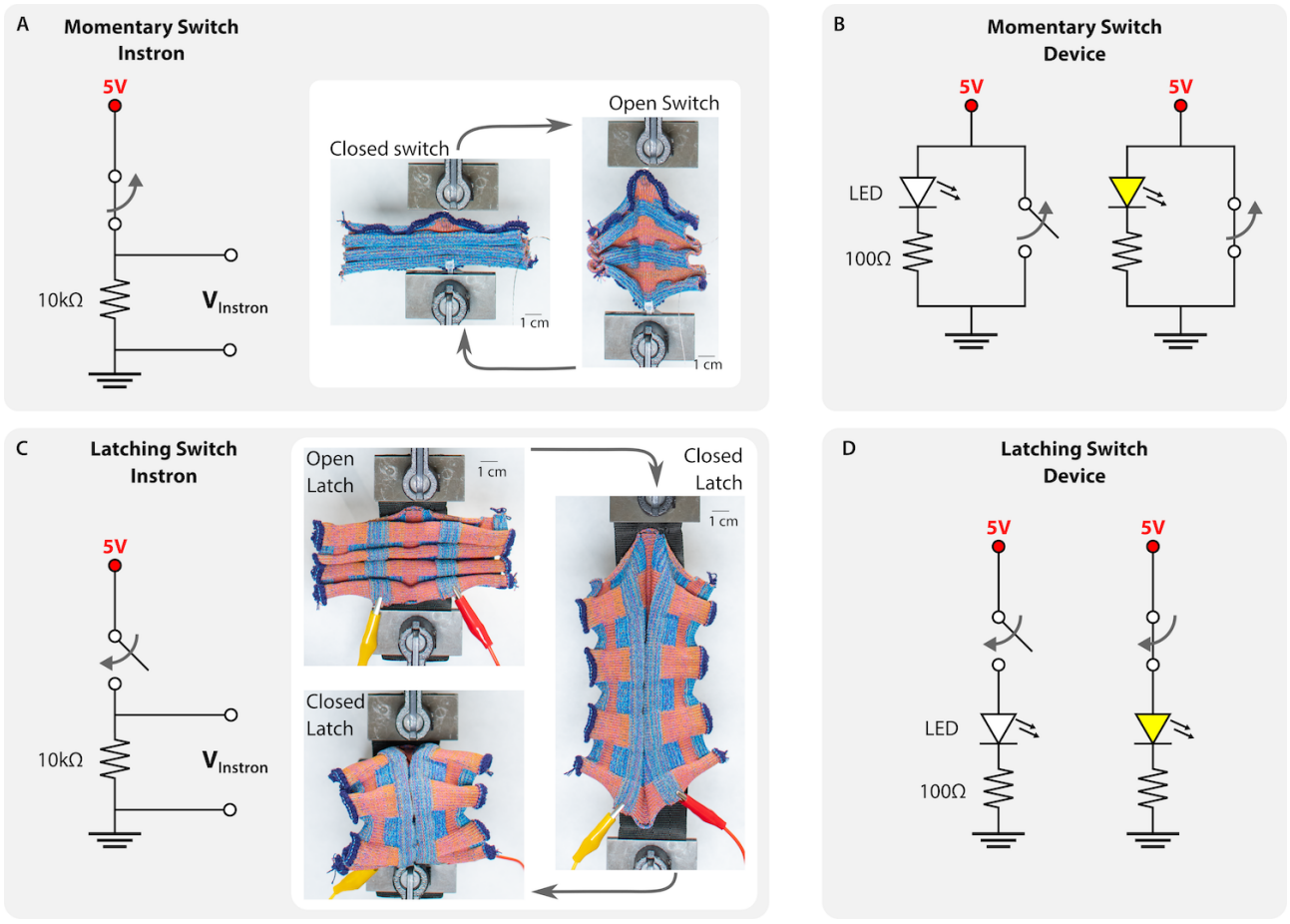


Figure S4: Circuit diagrams for the momentary (A,B) and latching (C,D) switches for measuring change in voltage in mechanical tests (A,C), and when integrated into wearable garments (B,D).

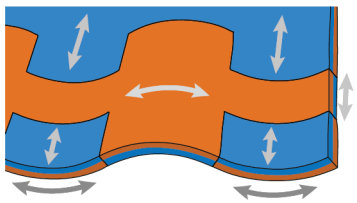


Figure S5: Directions of expansion in our bilayer simulation. The orange layer (technical face) expands in the x-direction, whereas the blue layer (technical back) expands in the y direction.

S4 Finite Element simulations

To demonstrate that the unique curvature and mechanical response of the considered knits are determined by the pre-stresses introduced during manufacturing, we performed Finite Element (FE) simulations using the commercially available software Abaqus 2021 [5]. Although developing numerical tools capable of accurately capturing the behavior of textiles remains an ongoing challenge, we show here that a simplified bilayer shell model can effectively elucidate the fundamental mechanisms driving the mechanical response of the knits under consideration.

All models are composed of an initially flat rectangular slab discretized with 4-node quadrilateral shell elements featuring hourglass control and reduced integration (S4R elements). Each model includes a composite bilayer section. The internal stresses arising from the knitting process are replicated in the simulation by assigning different coefficients of thermal expansion to the two layers. Specifically, both layers share identical linear elastic material properties but differ in their thermal expansion coefficients: $(\alpha_x, \alpha_y) = (0.165\ 1/C, 0)$ for the orange layer (technical face) and $(\alpha_x, \alpha_y) = (0, 0.0198\ 1/C)$ for the blue layer (technical back) in Fig. S5.

Due to the instabilities triggered during the simulations, the finite-sized samples were analyzed using a nonlinear dynamic implicit procedure (*DYNAMIC) under quasi-static conditions. Rayleigh damping was applied with proportional mass damping defined by a coefficient of $\alpha_r = 4$ for the thermal expansion step. For the subsequent point loading step this damping was scaled based on the approximate experimental time ($\alpha_r = 1400$). Critically, it is noted that the multistability of all samples is highly dependent on this damping parameter and can be tuned to occur even in the Step sample by reducing this damping value. No nodal imperfections were introduced, as the natural asymmetric pre-stress across the shell section was sufficient to initiate the deformation. For reference, all relevant codes are available in the accompanying GitHub repository (link). Each simulation consisted of two steps:

Step 1: Thermal Expansion

In the first step, the temperature is increased by one degree, generating internal stresses and curvature. The temperature change serves to replicate the internal stresses introduced during manufacturing. To ensure uniform thermal contraction, periodic boundary conditions were applied along the cell boundaries [6, 7].

When subjected to thermal loading, the shell models buckle out of plane, forming curved profiles as illustrated

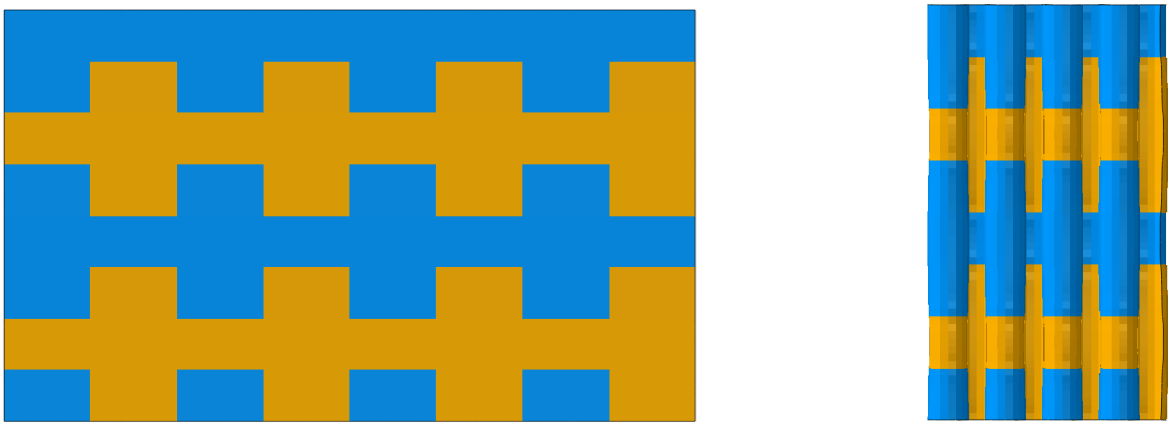


Figure S6: FEM contraction and curving of the knit simulated H-shaped pattern in response to thermal loads.

in Fig. S6. The resulting curvature of the simulated models depends primarily on the thermal expansion coefficients and the thickness of the shell section. In this study, the thermal expansion coefficients of the two layers (α_x, α_y) were adjusted to match the curvature observed in the manufactured knitted samples. The specific thermal expansion values used for each sample are listed in Table S2.

Table S2: Orthogonal thermal expansion coefficients for each sample geometry.

Sample Type	Orange layer $[\boldsymbol{\alpha_x}, \boldsymbol{\alpha_y}]$ (C^{-1})	Blue layer $[\boldsymbol{\alpha_x}, \boldsymbol{\alpha_y}]$ (C^{-1})
H-shaped	[0.165, 0]	[0, 0.0198]
Windmill	[0.04, 0]	[0, 0.165]
Step	[0.04, 0]	[0, 0 .105]

Step 2: Mechanical Loading

In the second step, a mechanical load is applied to the model. To replicate the boundary conditions of the finite-sized samples shown in Fig. 2, the periodic boundary conditions are first removed, and the model is allowed to relax. After relaxation, a displacement is gradually applied to a few boundary nodes (point loading) to reproduce the experimental conditions depicted in Fig. 2.

Numerical results

Three rib-garter patterns were simulated as finite sized bi-layer equivalents for the H-shaped, Windmill, and Step patterns shown in Fig. 2. The strain-energy of each sample during loading is shown in Fig. S7 alongside their configuration at the end of step 1 (labeled as unstretched) and step 2 (labeled as stretched). Critically, in the H-shaped model we see a clear strain energy minimum at a displacement of ~ 90 mm, which corresponds to a second energy minimum in the sample and highlights the bilayers role in creating multistability. The same

energy minimum is not observed in the Step sample. Finally, the Windmill model exhibits a shallow minimum at a displacement of approximately 20 mm.

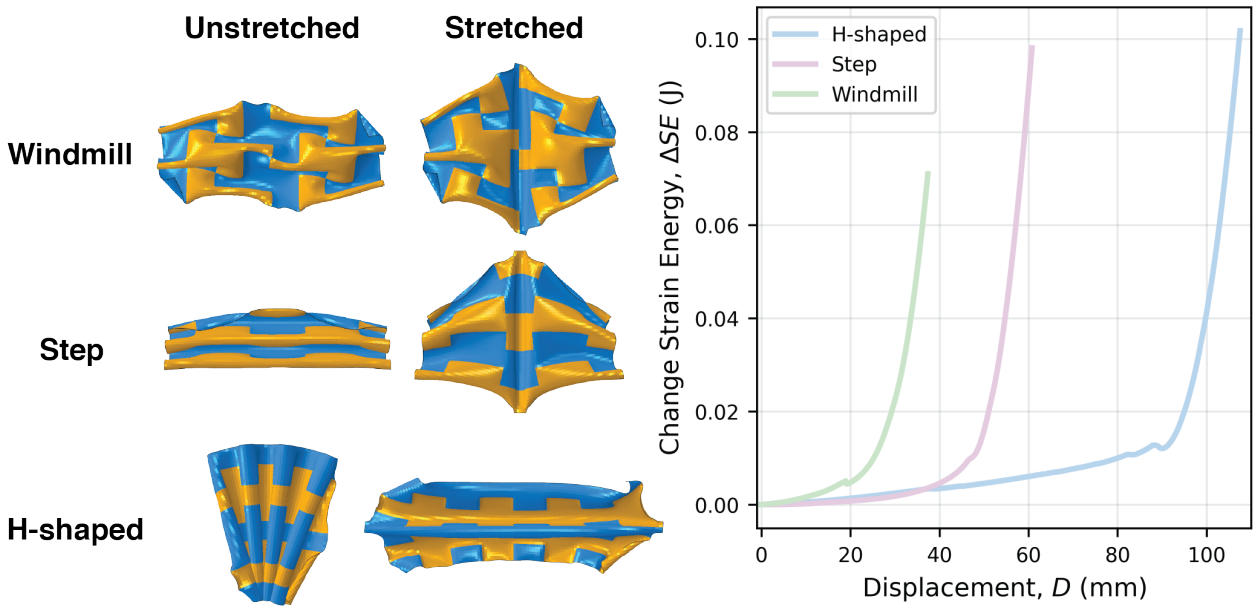


Figure S7: FEM strain energy results during point loading of three simulated geometries.

In Figure S8 we compare the numerically predicted (dashed line) and experimentally measured (continuous lines) force-displacement curves for the H-shaped, Step, and Windmill pattern. We find good agreement between the two sets of data. In full agreement with the experiments, the numerically predicted force-displacement curve for the H-shape pattern shows two force drops between 85 and 100 mm of displacement (highlighted by the grey circles) , after which the response stiffens as the shell becomes fully unfurled. For the Step pattern, both experimental and FE results show that there is no force drop, and stiffen at the sample displacement. Finally, both the FE and experimental results for the Windmill pattern show a force drop at similar displacements, and a subsequent stiffening.

In these simulations, we use a homogenized textile model to replicate the curvature and multistability of the knit samples through geometry and a pre-stressed bilayer. This type of homogenized model can help to understand system mechanics [7, 8], while avoiding the challenging and unresolved scaling complexity of yarn-level modeling [9]. These models are simplifications of reality and can never be perfectly accurate. For example, we predict that the yarn on yarn friction in the textiles is the cause of energy dissipation, but this dissipation is approximated with a finite element damping parameter. More accurate damping in simulation might lead to a better representation of the steep force drop.

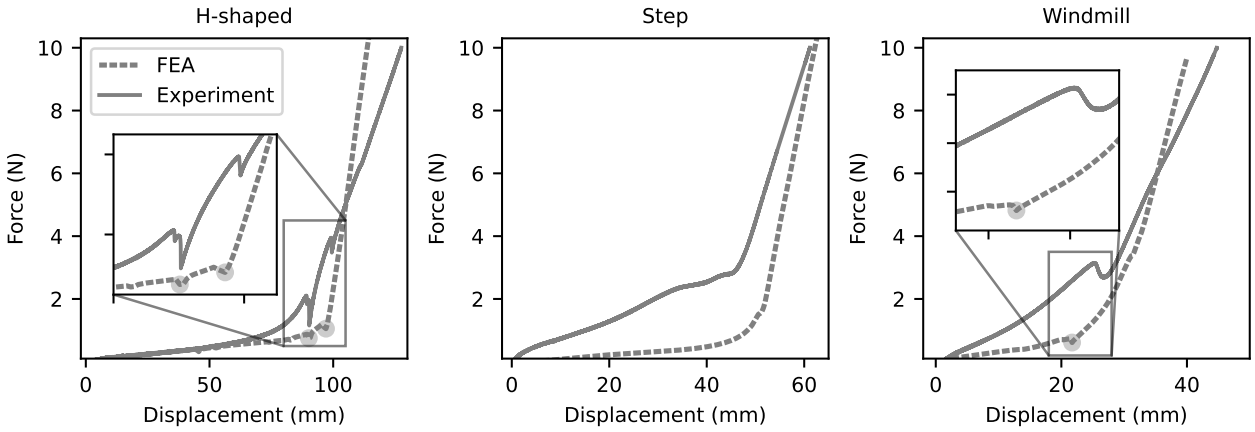


Figure S8: Comparison of the numerical predicted and experimentally measured force-displacement curves for the H-shaped, Step, and Windmill patterns. We also include insets to show in detail the force-drop in the FE results.

S5 Additional Results



Figure S9: A larger sample of jersey knit fabric shows the curling concentrated at the edges. Sample is approximately 10cm wide.

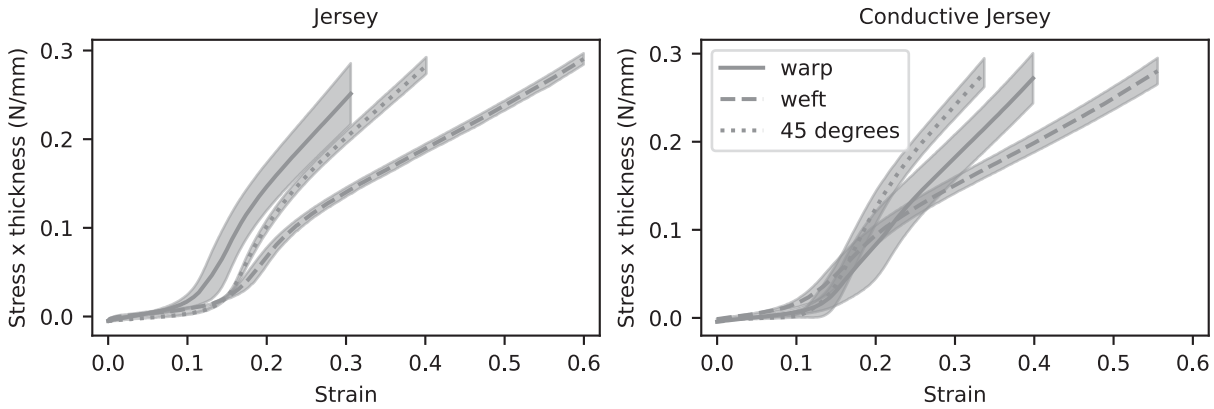


Figure S10: A) Mechanical response of a uniform, or jersey, fabric. Test samples were cut out of a larger textile so that the edges did not interfere. B) Mechanical response of a jersey fabric with two additional conductive yarns.

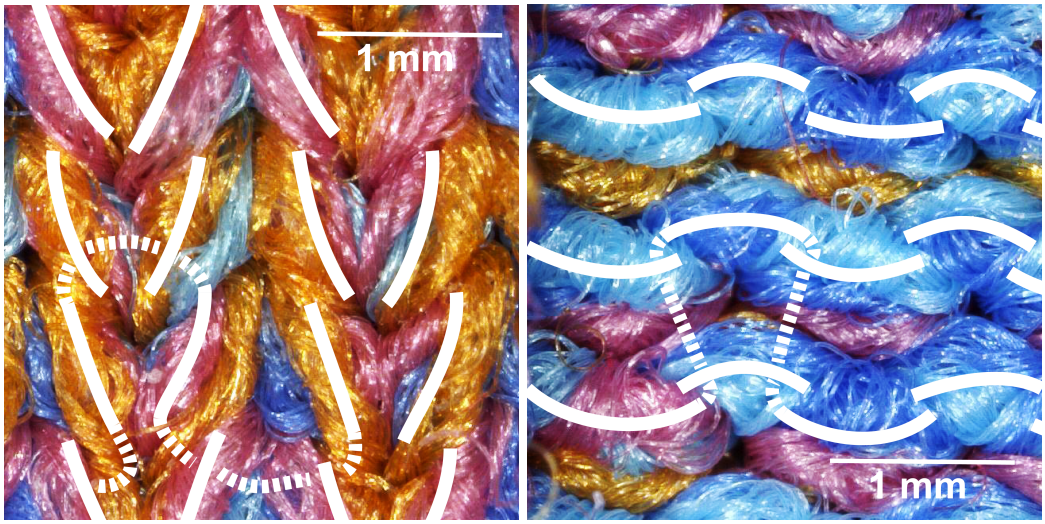


Figure S11: Microscope images show the face and reverse of the knit fabric. The paths of the yarns are sketched on top, where the paths of the yarns that are on the opposite side are shown in dotted lines. This sketch shows us that the yarns on the face lie mostly vertical and yarns on the reverse side lie mostly horizontal, with the crossovers happening through the thickness of the fabric.

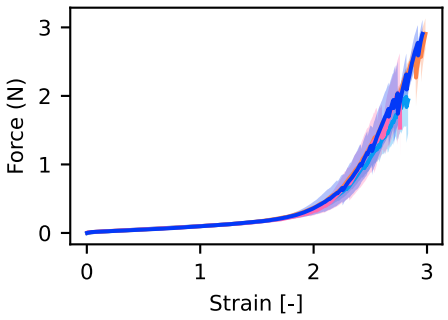


Figure S12: Mechanical response of all four elastomeric yarns. We observe that the color does not affect the mechanical response

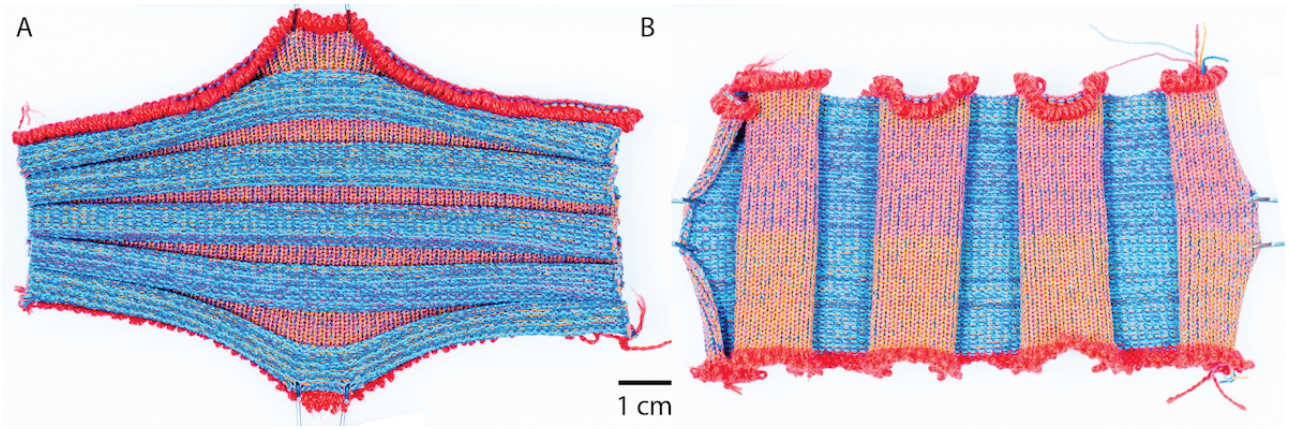


Figure S13: Rib and garter patterns are defined by the number of stitches in each stripe. Therefore a 12 x 12 pattern consists of 12 stitches knit on the front bed and 12 on the back bed. A) Top-down view of a 12 x 12 garter stitch, loaded at a single point to show both higher and lower strain regions. B) Top-down view of a 12 x 12 rib stitch, loaded at a single point to show both higher and lower strain regions. Top down views allow us to see the stripe patterns that define rib and garter knit patterns. Since each knit stitch is wider in the weft direction, the rib stripes are wider than those in the garter.

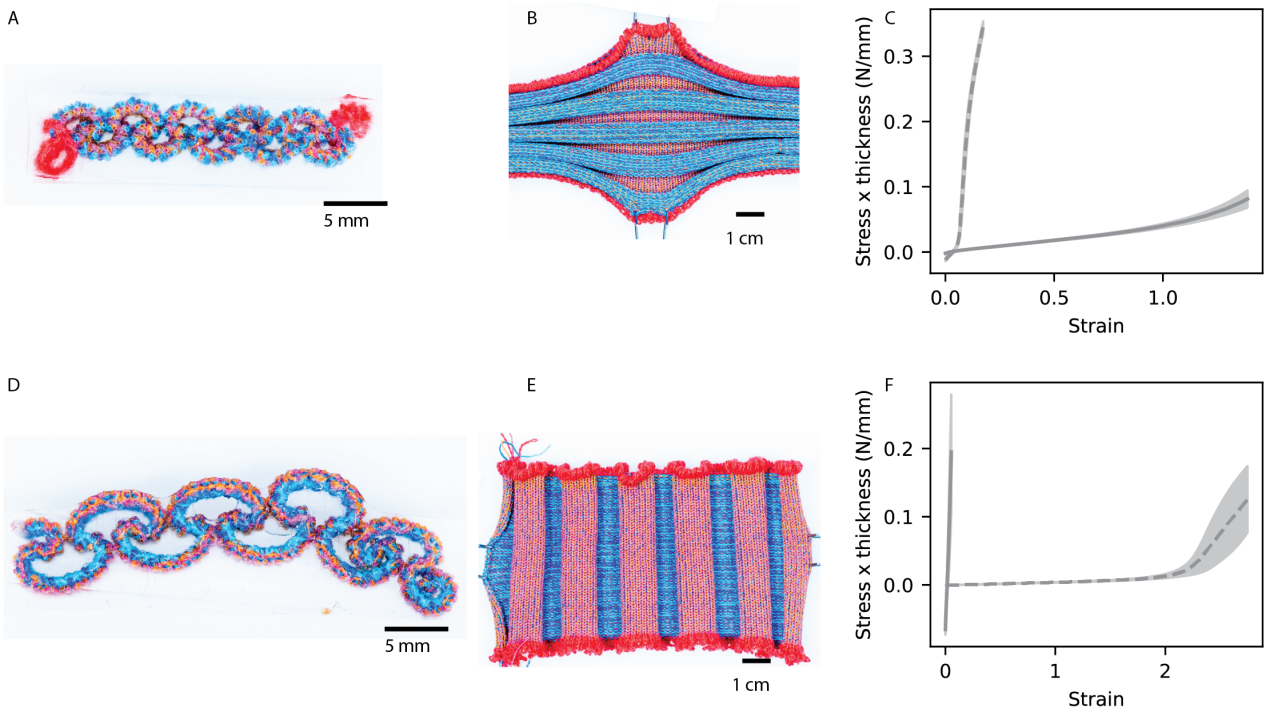


Figure S14: A) A cross section of an 8 x 8 garter pattern showing the corrugation and individual yarns. B) A top view of an 8 x 8 garter under a point load shows the textile under strain close to the center, and with no strain at the edges. C) Stress-strain curves of 8 x 8 garter in the warp and weft direction D) A cross section of an 8 x 8 rib pattern showing the corrugation and individual yarns E) A top view of an 8 x 8 rib under a point load shows the textile under strain close to the center, and with no strain at the edges. F) Stress-strain curves of 8 x 8 rib in the warp and weft direction

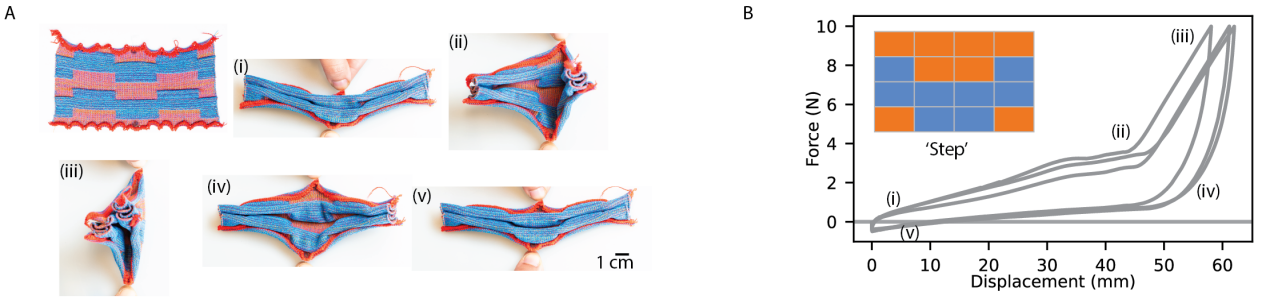


Figure S15: Additional photos and data for the *Step* unit cell. A) Photos of the sample at various displacements, which are marked on B. B) Force-displacement response of sample. Photos at displacements (i) - (iv) are displayed in A

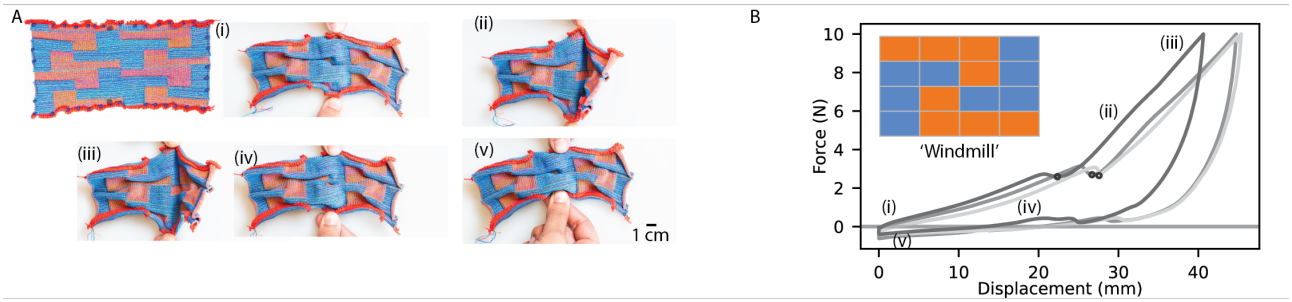


Figure S16: Additional photos and data for the *Windmill* unit cell. A) Photos of the sample at various displacements, which are marked on B. B) Force-displacement response of sample. Photos at displacements (i) - (iv) are displayed in A

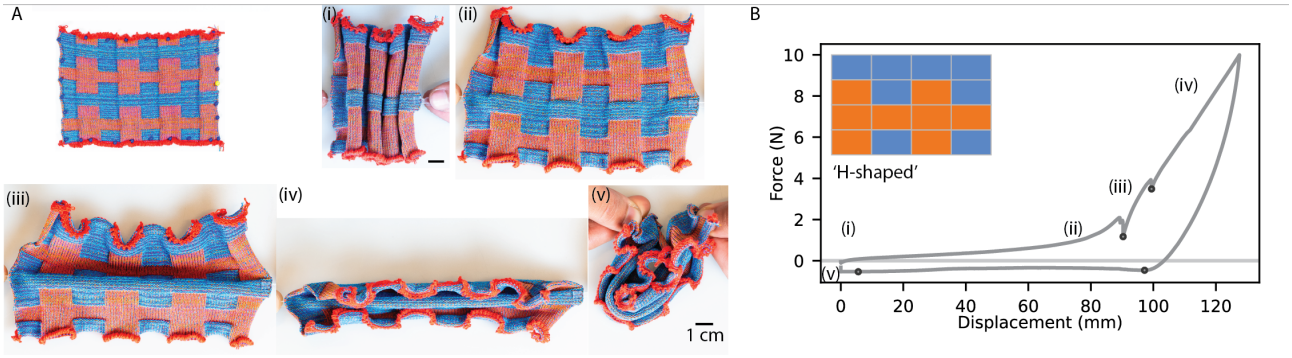


Figure S17: A) Additional photos for the *H-shaped* unit cell. A) Photos of the sample at various displacements, which are marked on B. B) Force-displacement response of sample. Photos at displacements (i) - (iv) are displayed in A. Further force-displacement data is shown in S24.

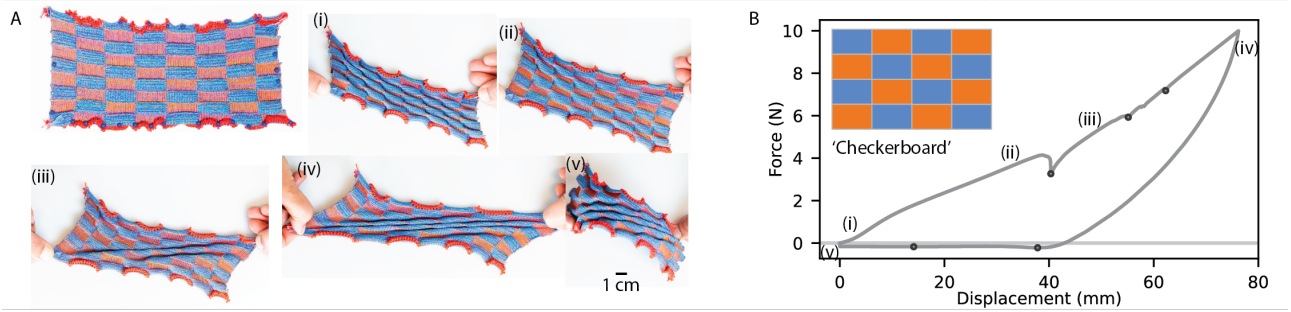


Figure S18: Photos and data for the *Checkerboard* unit cell. This knit pattern displays an unusual pattern of diagonal folds, which can fold either tilted left or right. The two possible fold directions allow for multistability. A) Photos of the sample at various displacements, which are marked on B. B) The force-displacement response for the checkerboard pattern when it is loaded along the diagonal direction. Photos at displacements (i) - (iv) are displayed in A

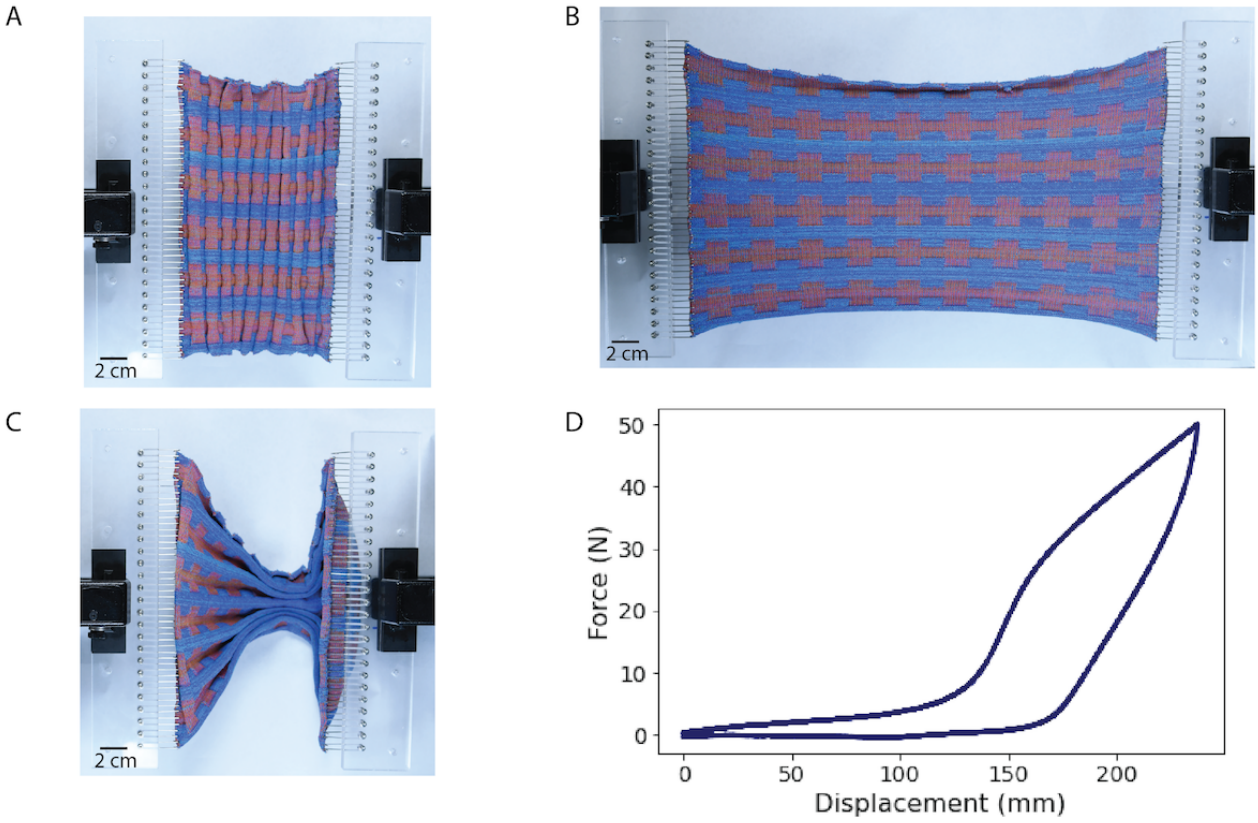


Figure S19: A) A larger sample of *'H-shaped'* unit cells is clamped along the edges. B) Strain is applied to the sample. C) When unloaded, the unit cells in the center of the sample have switched configurations. D) The force-displacement response of this clamped sample.

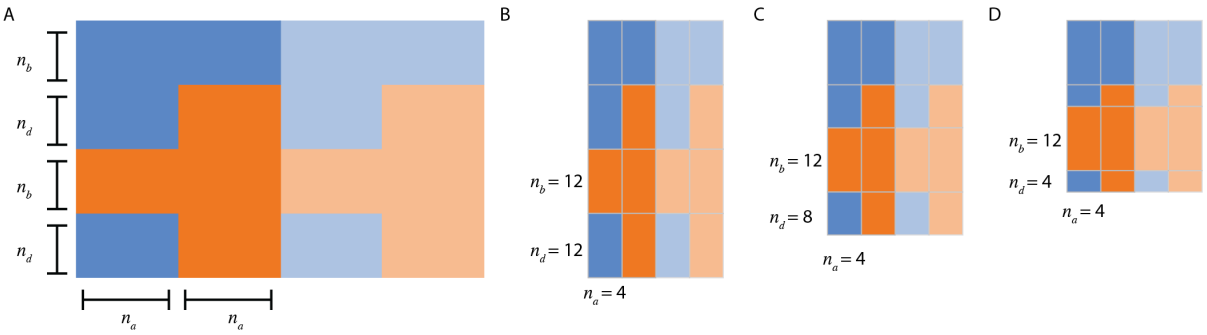


Figure S20: A) The 4 x 4 unit cell is made up of two identical 4 x 2 sections. This unit cell can be characterized by six parameters, which we reduce to three to maintain symmetry. B) A schematic of the sample shown in Fig. 5C-i. C)) A schematic of the sample shown in Fig. 5C-ii.) A schematic of the sample shown in Fig. 5C-iii.

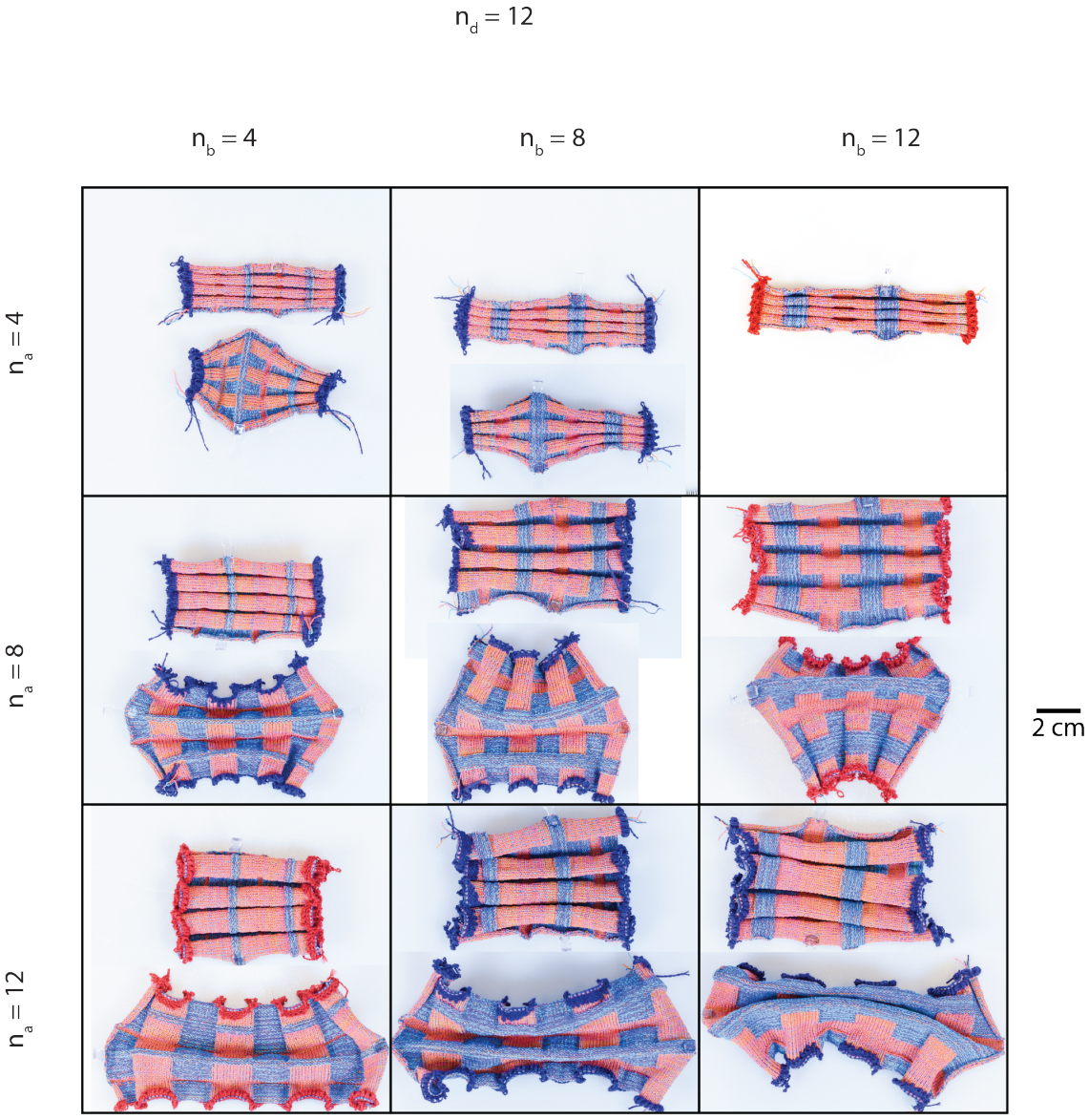


Figure S21: Photos of samples with *H-shaped* unit cells where $n_d = 12$.

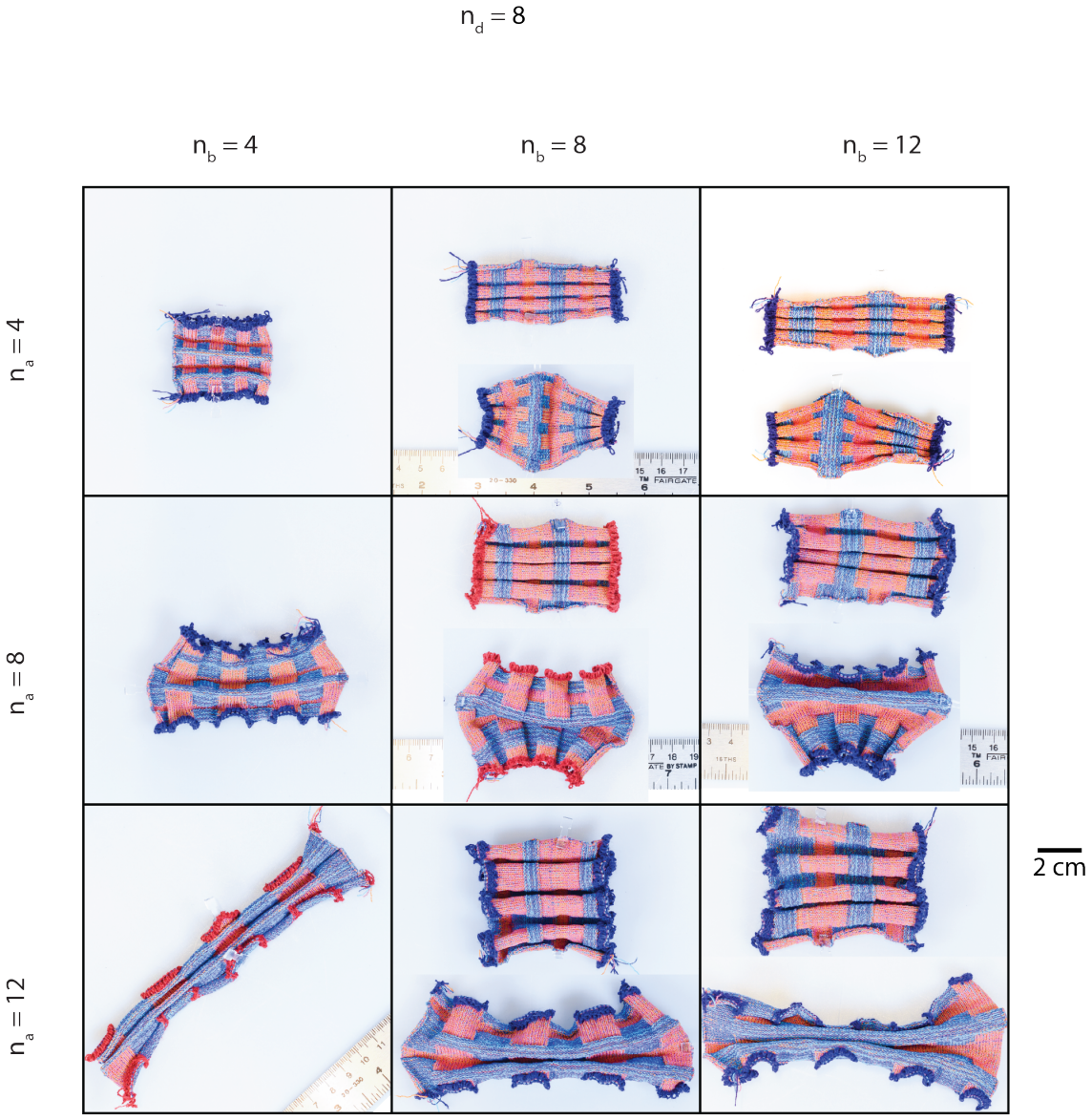


Figure S22: Photos of samples with *H-shaped* unit cells where $n_d = 8$.

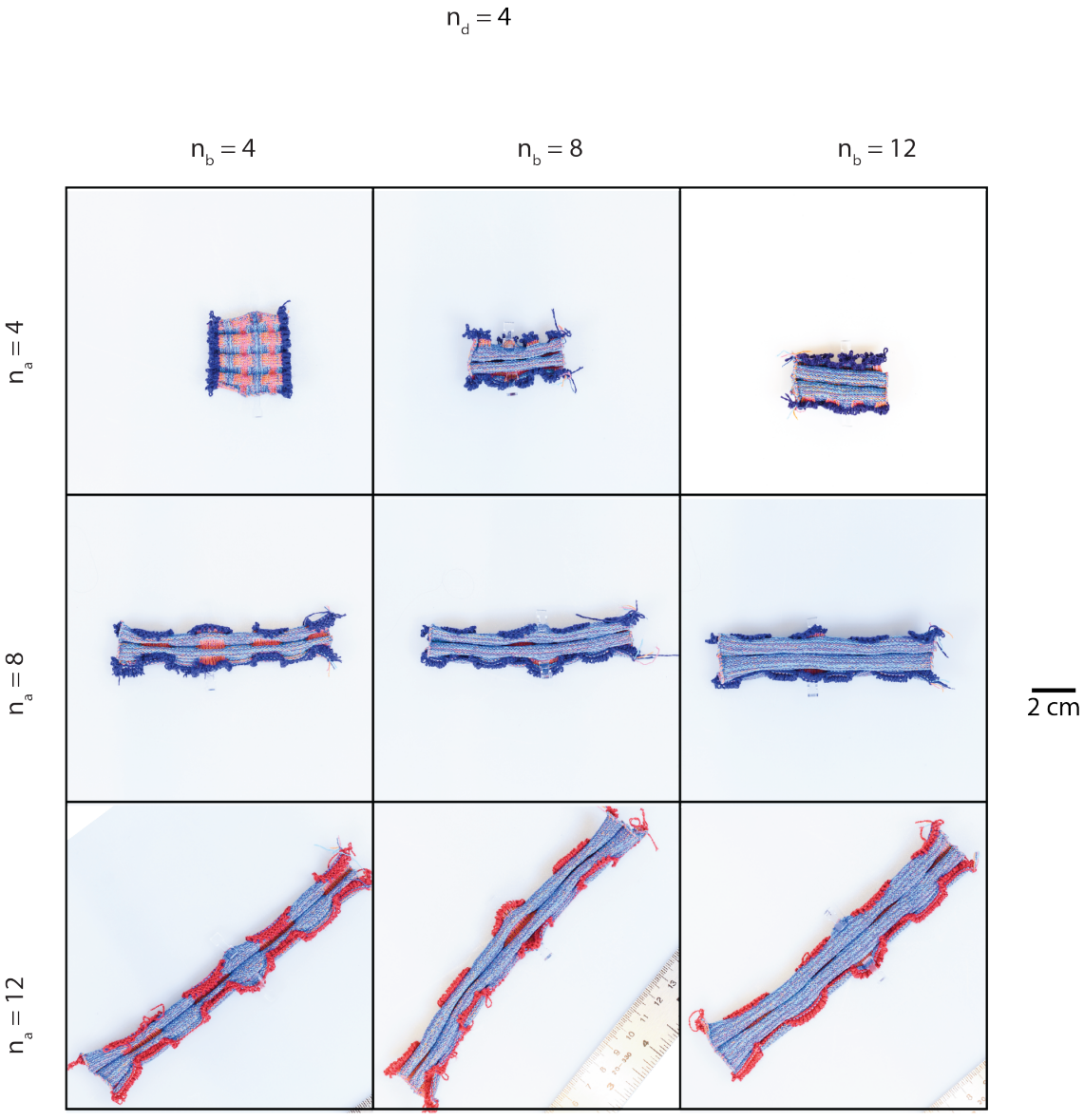


Figure S23: Photos of samples with *H-shaped* unit cells where $n_d = 4$.

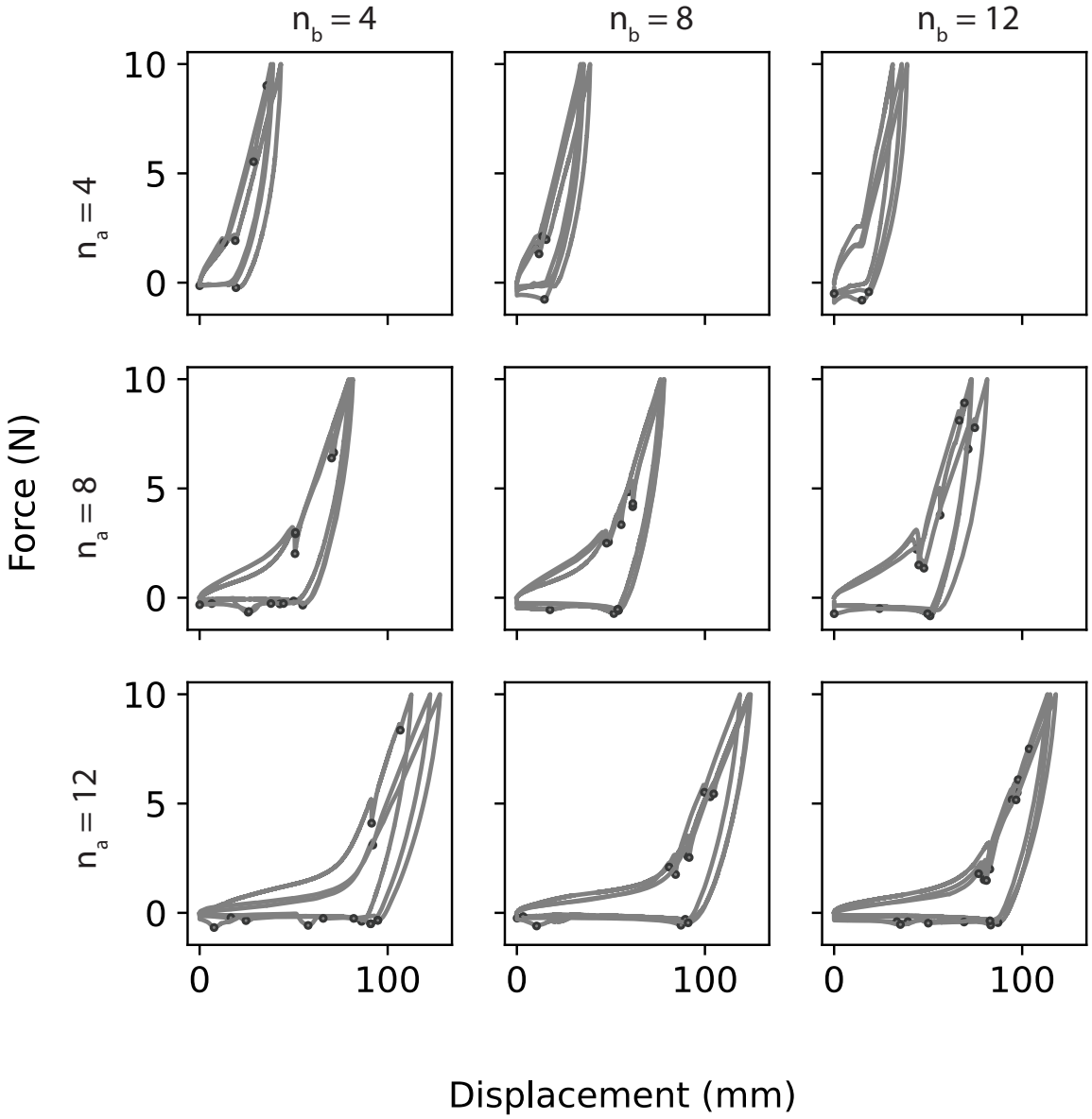


Figure S24: Additional data of samples with *H-shaped* unit cells where $n_d = 12$.

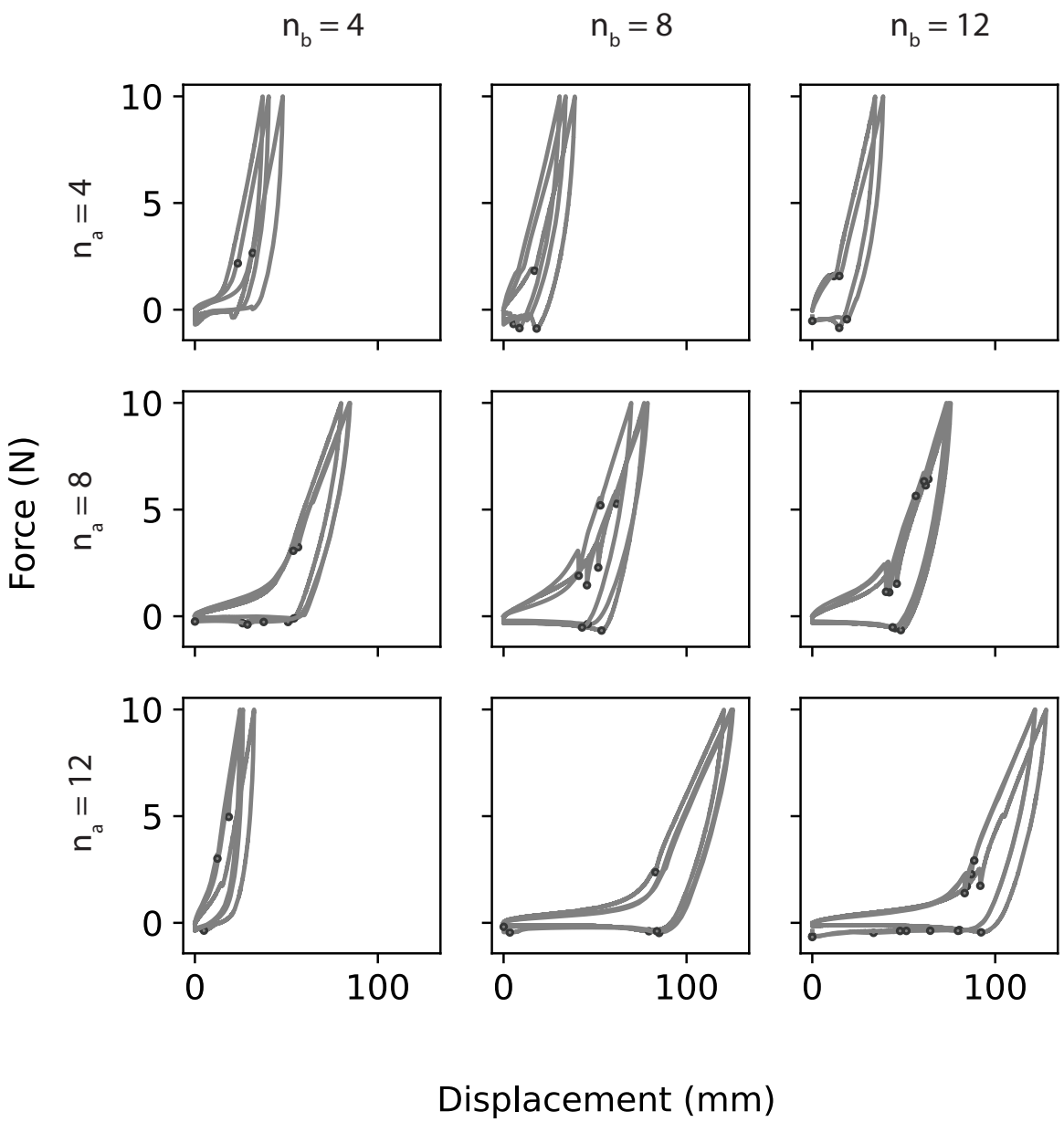


Figure S25: Additional data of samples with *H-shaped* unit cells where $n_d = 8$.

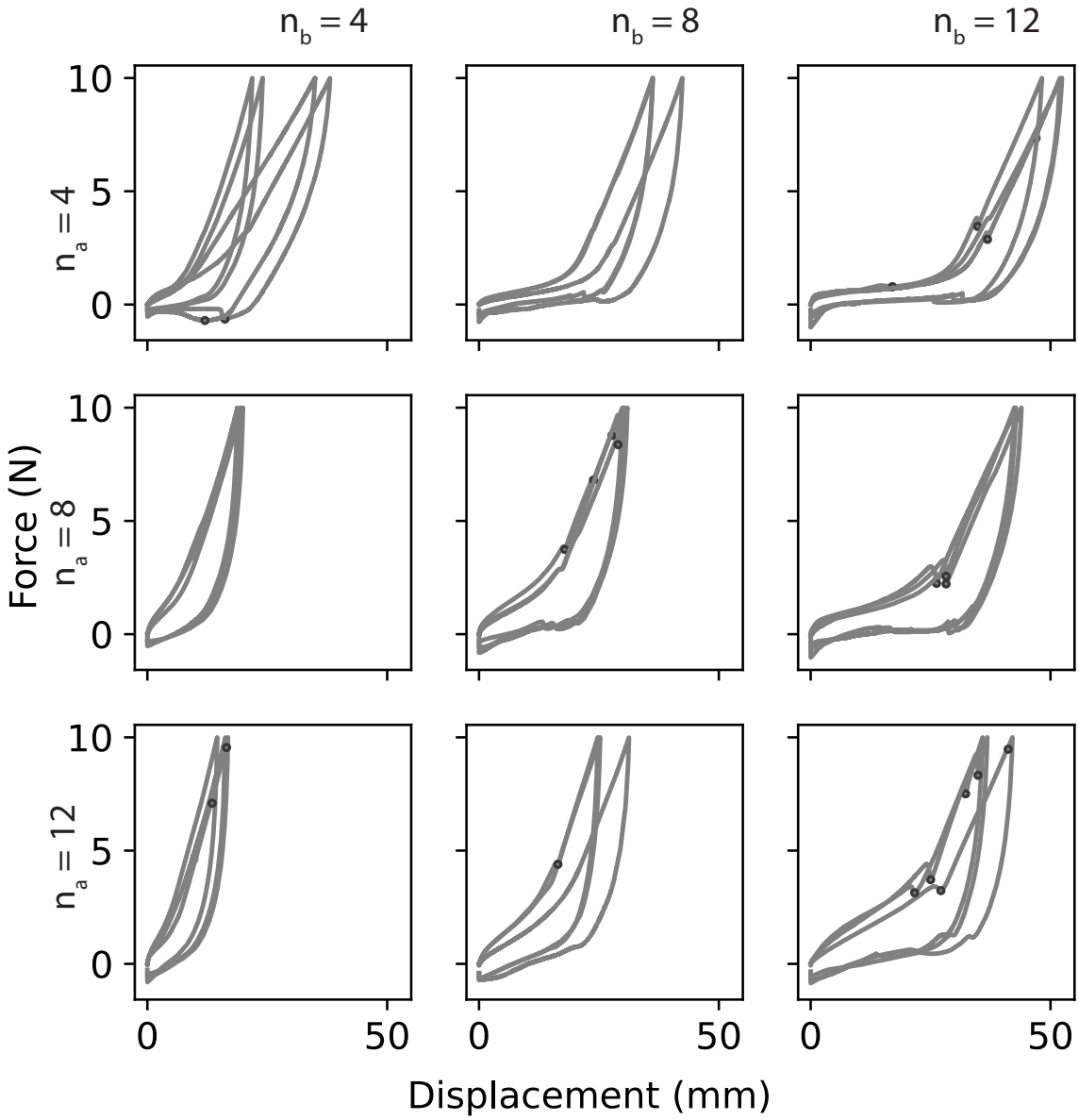


Figure S26: Additional data of samples with *H-shaped* unit cells where $n_d = 4$.

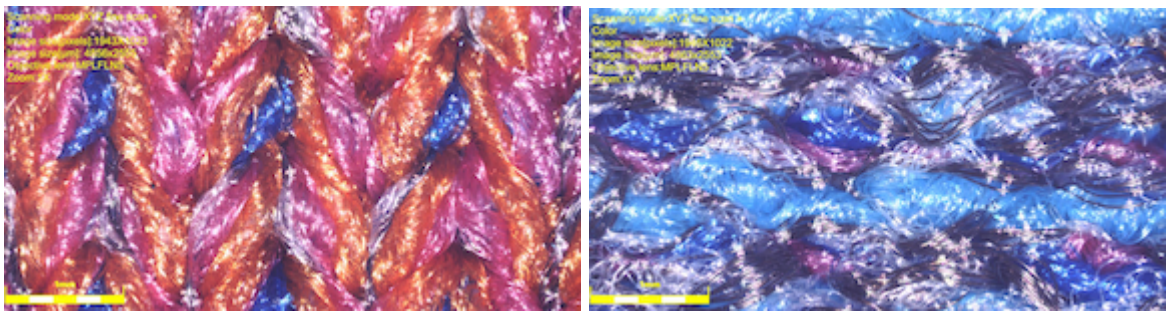


Figure S27: Microscope images show the front and back of the knit fabric which includes conductive yarns. The silver-plated yarns are visible between the orange and blue yarns. Scale bars are 1 mm.

S6 Movies

Movie S1: Knit structures under tensile loading

Movie S2: Knit switches with built-in haptic feedback

Movie S3: Applications of a momentary switch

Movie S4: Reconfigurable latching switch lamp

References

[1] Ohlson, G., Bonilla Fominaya, A. M., Puthuveetil, K., Wang, J., Amspoker, E., and McCann, J. In *Proceedings of the 8th ACM Symposium on Computational Fabrication*, 1–9, (2023).

[2] Narayanan, V. and McCann, J. `https://github.com/textiles-lab/knitout-frontend-py`, (2021).

[3] Narayanan, V., Ohlson, G., and McCann, J. `https://github.com/textiles-lab/knitout-backend-kniterate`, (2021).

[4] Sanchez, V., Mahadevan, K., Ohlson, G., Graule, M. A., Yuen, M. C., Teeple, C. B., Weaver, J. C., McCann, J., Bertoldi, K., and Wood, R. J. *Advanced Functional Materials* , 2212541 (2023).

[5] Dassault Systèmes Simulia Corp. *Abaqus 2021 Documentation*, (2021).

[6] Danielsson, M., Parks, D., and Boyce, M. *Journal of the Mechanics and Physics of Solids* **50**(2), 351–379 (2002).

[7] Farrell, D. T., McCann, C. M., Forte, A. E., Walsh, C. J., and Bertoldi, K. *Advanced Materials* , e2505817 (2025).

[8] Connolly, F., Walsh, C. J., and Bertoldi, K. *Proceedings of the National Academy of Sciences* (2016).

[9] Ding, X., Sanchez, V., Bertoldi, K., and Rycroft, C. H. *Proceedings of the Royal Society A* **480**(2295), 20230753 (2024).